

30 **Abstract**

31 The beginning of the Mid-Pleistocene Transition (MPT) ~920 ka BP marked the
32 expansion of northern hemisphere ice shields and caused a significant climate change
33 in NW Europe. The MPT ended with the establishment of the 100 kyr ice age cyclicity at
34 ~640 ka BP, due to orbital eccentricity changes. Previous studies explained the northern
35 hemisphere cooling by cooling of sea-surface temperatures, increased sea-ice cover
36 and/or changes in the Atlantic Meridional Overturning Circulation (AMOC) strength. We
37 here discuss very-high resolution parametric echosounder (Parasound) imagery and
38 sediment core analytics from a plastered drift at the eastern Campeche Bank (southern
39 Gulf of Mexico), which was deposited under the influence of the Loop Current (LC). The
40 LC transports warm tropical waters from the Caribbean into the Gulf via the Yucatan
41 Channel. It is a key component of the Gulf Stream system, driving the ocean heat,
42 salinity, and moisture transport towards the N Atlantic. The joint interpretation of
43 reflection patterns, age constraints from color-scanning, foraminiferal stable oxygen
44 isotopes, Sr isotope ratios ($^{87}\text{Sr}/^{86}\text{Sr}$) and core-seismic integration led to consistent
45 conclusions about changes in LC strength across the MPT, thereby modulating the deep
46 base level and the deposition of the plastered drift. The development of offlapping or
47 onlapping plastered drifts, or the transition between the two termination patterns is best
48 explained by changes in the depth of the relative deep base level and interpreted by
49 changes in the flow regime.

50 Initially, the Middle Miocene to Pliocene closure of the Central American Seaway caused
51 the onset and intensification of the LC and hence a deep base level fall. The sedimentary
52 deposits from this phase have an offlapping prograding clinoform configuration,
53 resembling a forced regression systems tract as is known from shelf areas. The deep
54 base level fall caused sediment truncation above 500 m present day water depth. Below
55 500-550 m, the offlapping succession is overlain by sigmoidal and onlapping,
56 transgressive systems tract like clinoforms. The transition from deep base level fall prior
57 to the MPT to deep base level rise documents the weakening of the LC during the early
58 MPT. After the MPT, the LC continued to weaken. The related reduction of heat transport
59 from the Western Atlantic Warm Water Pool into the North Atlantic contributes to the
60 further cooling of the northern hemisphere. Generally, the development of offlapping or
61 onlapping plastered drifts or the transition between the two termination patterns can be
62 explained by changes in the depth of the relative deep base level and interpreted by
63 changes in the flow regime.

64 **Keywords**

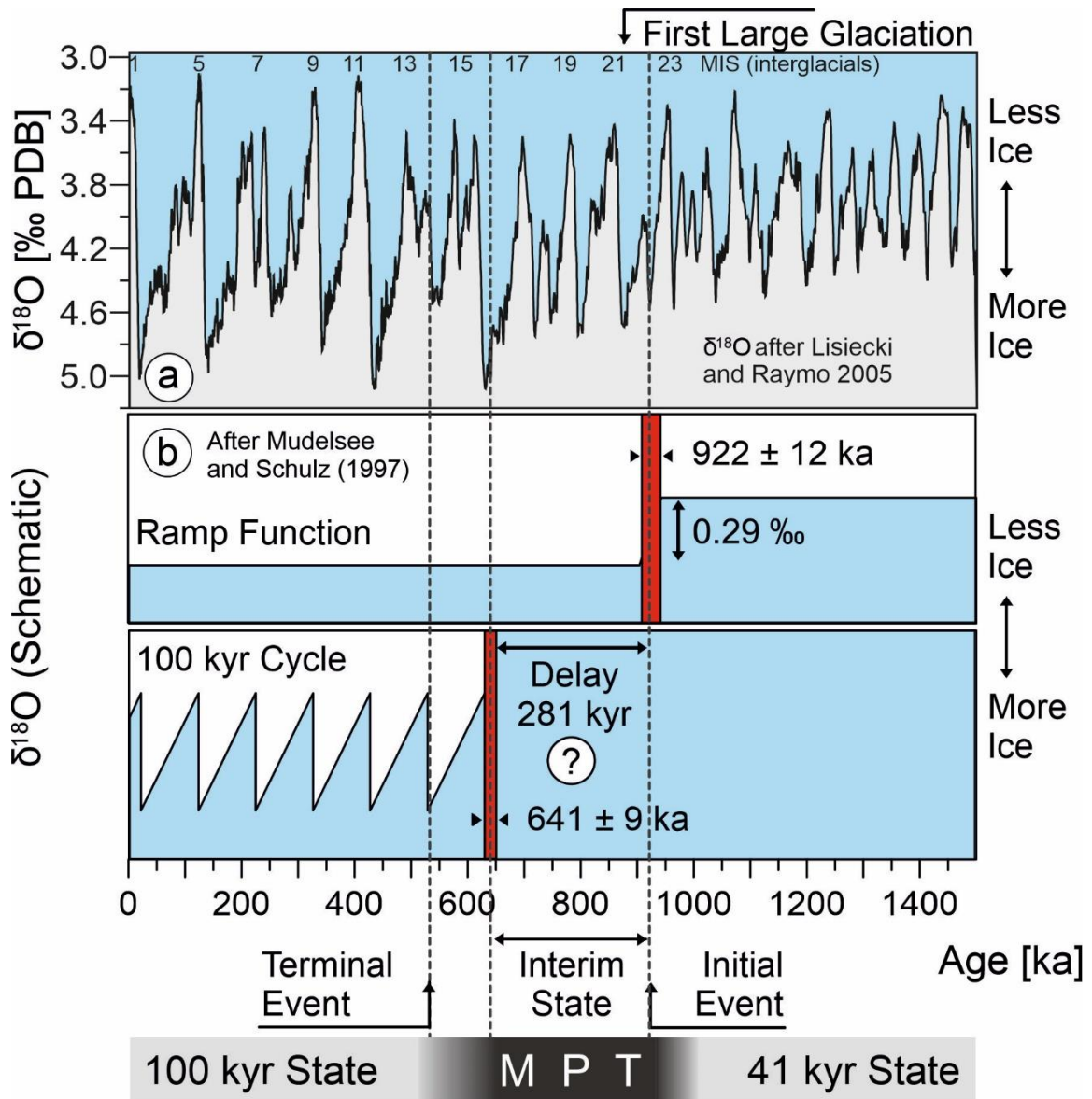
65 Gulf of Mexico, paleoceanography, seismic, micropaleontology, plastered drift,
66 Chicxulub impact

67

68 **1. Introduction**

69 The Atlantic meridional overturning circulation (AMOC) influences the North Atlantic
70 hydrography, heat balance, and finally the climate in NW Europe (Schott et al., 1988;
71 Molinari et al., 1990; Schmitz and Richardson, 1991; Nürnberg et al., 2008). The
72 expansion of northern hemisphere ice shields at the beginning of the Mid-Pleistocene
73 transition (MPT) ~920 ka BP (Mudelsee and Schulz, 1990) caused a significant climate
74 change in NW Europe. The MPT ended with the establishment of the 100 kyr ice age
75 cyclicity at ~640 ka BP, caused by orbital eccentricity changes (Pisias and Moore, 1981;
76 Prell, 1982; Ruddiman et al., 1989) (Fig. 1). The reason for the 280 kyr delay of 100 kyr
77 cyclicity remains enigmatic. The neglectable variability of orbital forcing cannot account
78 alone for the dominance of 100 kyr-period oscillations in the climate system (Imbrie et
79 al., 1993).

80 Several proxys implied significant changes in the deep-water circulation in association
81 with the MPT (for an overview see Tachikawa et al., 2020, and references therein).
82 Schmieder et al. (2000), for example, concluded from a high-resolution Pleistocene
83 magnetic susceptibility time series from the subtropical South Atlantic that dissolution
84 driven variations in carbonate accumulation were controlled by deep water circulation
85 changes. They assumed that the MPT was a discrete state of the Pleistocene deep-
86 water circulation and climate system, terminated at ~540-530 ka. Nd isotope analysis by
87 Pena and Goldstein (2014) pointed to a major disruption of the South Atlantic
88 thermohaline circulation (THC) system during the MPT between Marine Isotope Stage
89 (MIS) 25 and MIS 21 from ~950 to ~860 ka BP, with a significant weakening during MIS
90 23 (~900 ka BP). After the MPT, the glacial deep-water circulation continued to remain
91 relatively weak during the glacials. Kim et al. (2021) also used Nd isotopes to confirm
92 this interpretation for the North Atlantic, proving that this “MPT-AMOC crisis” occurred
93 basin wide. Pena and Goldstein (2014) stated that the MPT ocean circulation crisis
94 facilitated the coeval drawdown of atmospheric CO₂ (Hönisch et al., 2009) and
95 subsequent high-latitude ice sheet buildup. Kaiser et al. (2019) concluded on enhanced
96 northward advection of warm water during MIS 22 to 21 by interpreting the coiling
97 direction of planktic foraminifer.

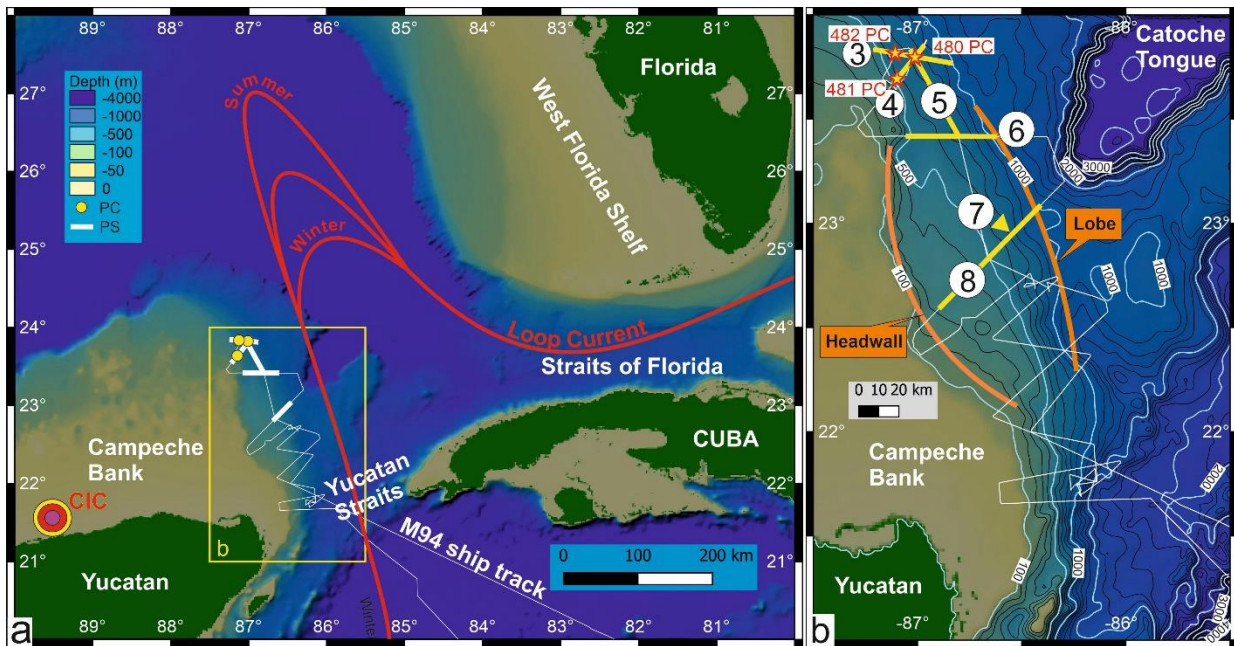


100 Fig. 1: Chronology of the Mid-Pleistocene climate transition (after Schmieder et al.
 101 2000). Shift in mean and lagged onset of 100 kyr cyclicity of global ice volume (a)
 102 reflected in the stacked $\delta^{18}\text{O}$ global reference record (Lisiecki and Raymo, 2005) and
 103 (b) schematic view of the Mid-Pleistocene Climate Transition schematized after
 104 Mudelsee and Schulz (1997).

107 The Loop Current (LC) as prominent component of both the western boundary current
 108 system of the North Atlantic and the basin- to global-scale meridional overturning system
 109 dominates the surface and subsurface circulation in the Yucatan Strait and the Gulf of
 110 Mexico (Sturges and Evans, 1983; Zavala-Hidalgo et al., 2006) (Fig. 2a). The LC exits
 111 the Gulf of Mexico through the Florida Straits before entering the North Atlantic (Johns

112 et al., 2002; Ezer et al., 2003; Oey et al., 2003; Oey 2004). As part of the Gulf Stream
113 system, the LC represents a key element of the AMOC.

114



115

116

117 *Fig. 2: (a) Bathymetric map of southern Gulf of Mexico with adjacent Yucatan and Florida*
118 *straits. The red lines indicate the simplified Loop Current during different seasons. Thin*
119 *white line indicates M94 track (Hübscher et al., 2013). CIC = Chicxulub impact crater*
120 *(Paull et al., 2014). (b) M94 cruise track (white lines), core sites (star symbols) and*
121 *seismic profiles 3-8 (yellow lines), which correspond to the figures 3-8. Isobaths are*
122 *plotted at 100 m intervals. PC = piston core; PS = Parasound. Bathymetric dataset:*
123 *ETOPO1 (Amante et al., 2009).*

124

125 Hübscher et al. (2010) studied the impact of LC-related bottom currents on the upper
126 slope sediments of the north-eastern Campeche Bank, Gulf of Mexico (Figs. 2a, 3).
127 Sediment subbottom profiler data revealed a prominent unconformity (or disconformity)
128 in water depth between 600 and ~680 m depth. They concluded that the transition from
129 wavy reflection patterns in the lower succession to parallel deposits above, separated
130 by a prominent unconformity, was caused by a change in LC strength at intermediate
131 water depths. At that time, the lacking time constraints did not allow to unequivocally link
132 LC variability to that of climate change.

133 This study is motivated by the working hypothesis that the inferred LC variability is
134 related to the MPT and that a close relationship exists between changes in THC strength

135 (Fig. 1) and LC vigor (i.e. Hübscher et al., 2010). The data and samples were collected
136 during RV METEOR expedition M94 in 2013 (Hübscher et al., 2014). Parametric
137 sediment sub-bottom profiler transects and piston cores collected along the Campeche
138 Bank (Fig. 2b) allow a detailed view on the temporal and spatial development of the
139 unconformity initially described by Hübscher et al., (2010) and hence, the evolution of
140 the Yucatan Strait throughflow since the MPT.

141

142 **2. Regional Setting**

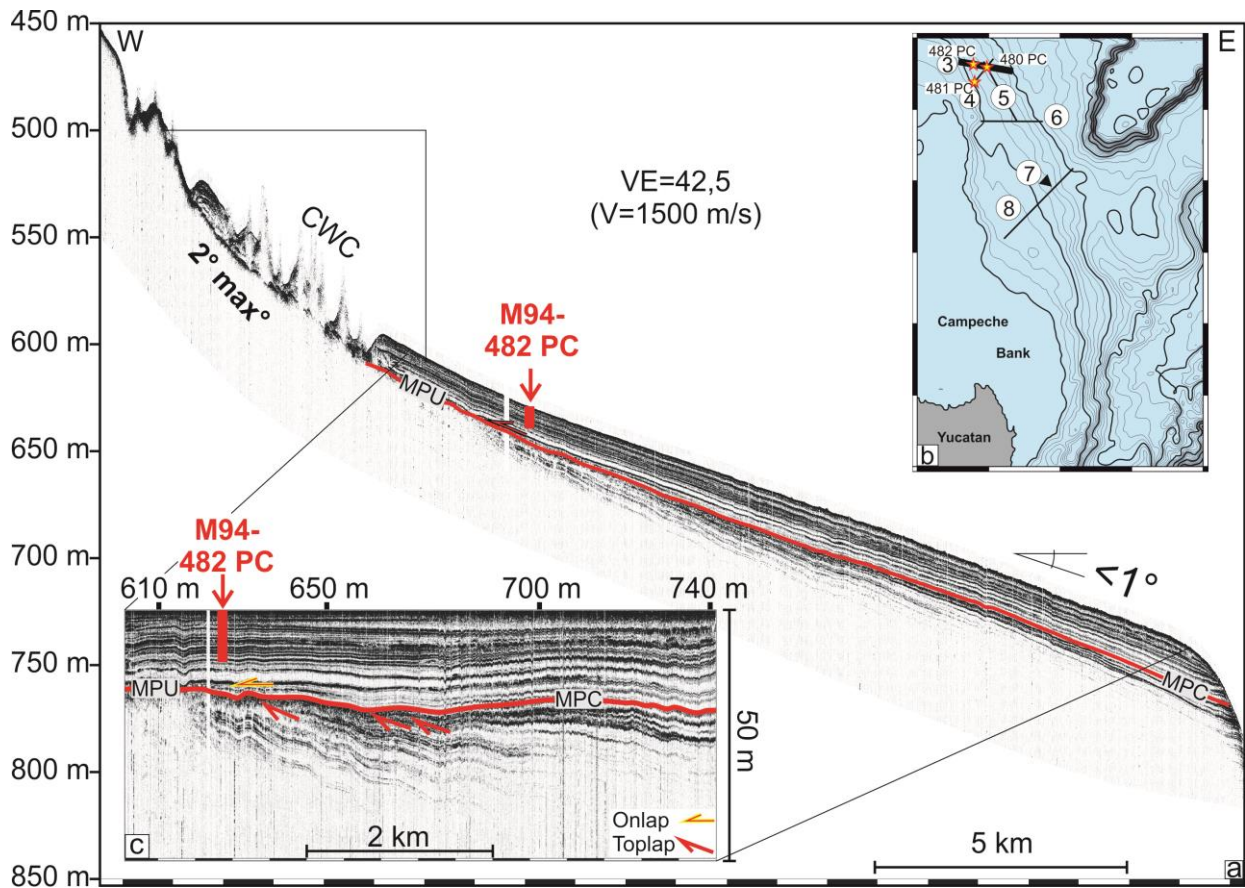
143 The Gulf of Mexico is a semi-enclosed basin, which is framed by wide and shallow
144 intertidal shelf areas (<20 m water depth; Fig. 2a). The study area is the north-eastern
145 and eastern Campeche Bank. This massive and broad carbonate bank located north of
146 the Yucatan Peninsula evolved until the mid-Cretaceous (Ordonez, 1936), and appears
147 geologically similar to the southern Florida platform (e.g., Antoine and Ewing, 1963;
148 Uchupi and Emery, 1968). Paull et al. (2014) related a steep cliff at the lower escarpment
149 of the northern Campeche Bank to the Chicxulub impact close to the Cretaceous–
150 Paleogene (K-Pg) transition. The joint interpretation of bathymetric maps and seismic
151 data provided a clear line of evidence that the impact caused catastrophic mass wasting
152 at the continental shelf adjacent to the escarpment due to the seismic shaking. Sanford
153 et al. (2016) mapped muddy debrites in the northern Gulf of Mexico and attributed them
154 to coastal and shallow-water environments, which were remobilized mainly at the Texas
155 shelf and northern margin of the Florida Platform throughout the Gulf of Mexico via
156 seismic and mega-tsunami processes initiated by the impact. These authors concluded
157 that the central and southern Florida Platform underwent a more localized platform
158 collapse. The impact did not only cause mass wasting, but also disrupted and fractured
159 upper-Cretaceous strata across the about 300 km wide western Florida shelf (Poag,
160 2017).

161 Near-surface sediments at the north-eastern Campeche Bank and the western Florida
162 Slope consist mainly of calcareous ooze with >75 % of carbonate (Balsam and Beeson
163 2003; Hübscher et al., 2014), being shaped by the different currents in the Yucatan
164 Channel between Yucatan and Cuba. Regarding the northbound flow, Sheinbaum et al.
165 (2002) distinguished between the northward flowing northerly surface Yucatan Current
166 and its southerly under-current off Mexico, and the southerly surface Cuban Counter-
167 current near Cuba. Within the Gulf of Mexico, the current system is termed LC.
168 Paleoceanographic proxy records from the area reveal a close relationship between the

169 LC dynamics, marine productivity, sea-surface temperature and salinity, and Mississippi
170 discharge on centennial to orbital timescales (Emiliani, 1975; Gardulski et al., 1990;
171 Nürnberg et al., 2008, 2015; Ziegler et al., 2008; Kujau et al., 2010).

172 Based on studies by Merino (1997), Rivas et al. (2005) and Hebbeln et al. (2014), Matos
173 et al. (2017) characterized the local oceanography by five water masses. The Caribbean
174 Surface Water (CSW) is transported northward at depths shallower than ~80 m. Below,
175 a salinity maximum at ~100–160 m water depth characterizes the core of the Subtropical
176 Intermediate Water. The Tropical Atlantic Central Water (TACW) exhibits an oxygen
177 minimum at ~500 m water depth. The salinity minimum identifies the upper boundary of
178 the Antarctic Intermediate Water (AAIW) at ~540 m water depth. The North Atlantic Deep
179 Water (NADW) is present at water depths deeper than 1000 m.

180 Hübscher et al. (2010) discovered a Cold Water Coral (CWC) province along the north-
181 eastern Campeche Bank (Fig. 3), mainly composed of *Enallopsammia profunda*-
182 *Lophelia pertusa*, which was subsequently mapped in detail between 23°47'N and
183 23°54'N (Hebbeln et al., 2014; Matos et al., 2017). The Campeche CWC province is
184 affected by the SE-NW directed LC (Fig. 1), which is strongest at surface (< 130 m water
185 depth; 74–83 cm/s), while its eddies reach much deeper (Hebbeln et al., 2014). At water
186 depths of ~500-600 m, the prominent Campeche CWC mounds occur, enduring bottom
187 velocities of ~30 cm/s (Hebbeln et al., 2014). A strong density gradient described at
188 ~520–540 m is attributed to the boundary (pycnocline) between TACW and AAIW
189 (Matos et al., 2017). Based on observed undulating isotherms, Hebbeln et al. (2014)
190 hypothesized on the presence of internal waves in that water depth. According to Matos
191 et al. (2017), the pycnocline was absent during the glacial time periods of substantially
192 lowered sea level.



193
 194
 195 *Fig. 3: (a) Parasound profile 3 collected during RV Meteor expedition M78/1 (Hübscher*
 196 *and Pulm, 2009) from eastern Campeche Bank (Hübscher et al., 2010) with location of*
 197 *piston core M94-482 PC. Core length has been calculated with a sound velocity of 1.5*
 198 *m/ms, which might be too low (see chapter 5 for discussion). (b) Bathymetric map of*
 199 *study area (see also Fig. 2b) (c) Flattened profile of lower eastern Campeche Bank slope*
 200 *(for explanation see Chapter 3). CWC = Cold-water coral; MPU = Mid-Pleistocene*
 201 *Unconformity; MPC = Mid-Pleistocene Correlated Conformity (MPC); VE = vertical*
 202 *exaggeration.*

203
 204 The Gulf of Mexico as the northern part of the western Atlantic warm water pool is an
 205 important oceanic heat source, providing ocean heat towards the North Atlantic via the
 206 Gulf Stream System, thus acting as a key area in the global climate system. The LC as
 207 part of the Gulf Stream system dominates the surface and subsurface flow in the Gulf of
 208 Mexico (Sturges and Evans, 1983; Zavala-Hidalgo et al., 2006) (Fig. 2a). It comprises
 209 warm tropical waters that flow from the Caribbean into the Gulf through the Yucatan
 210 Channel and some distance towards the north, before shedding anticyclonic eddies
 211 (e.g., Oey, 2008, and references therein). The northward flow is compensated by a deep

212 southbound counter flow into the Caribbean on both western and eastern lower slopes
213 of the Yucatan Strait (Sheinbaum et al., 2002).

214 Two endmember modes characterize the northward extension of the LC. During
215 summer, when the warm surface-water flow through the Yucatan Channel is enhanced,
216 the LC may even reach the Mississippi river delta (Wiseman and Dinnel, 1988;
217 Sheinbaum et al., 2002), thereby warming up the western and northern Gulf areas
218 (Brunner et al., 1984). During winter, the LC flows almost directly from the Yucatan
219 Channel to Florida Strait. During this phase, the northern Gulf remains rather unaffected
220 by warm tropical surface water from the Caribbean. According to Ezer et al. (2003), the
221 through-flow fluctuations in the Yucatan Channel largely correlate with the northward
222 spreading of the LC.

223

224 **3. Material and Methods**

225 **3.1 Bathymetry**

226 Bathymetric measurements were carried out mainly with the hull mounted SIMRAD
227 EM122 multi-beam system (Hübscher et al., 2014). This system emits periodically a
228 swath of 256 preformed beams with signal frequencies of 12 kHz. The usable footprint
229 of a single emitted swath perpendicular to the ship's heading has a width of larger than
230 three times of the water depth. Due to the shallow water depth and the large distances
231 between the profiles, the ETOPO1 data set (Amante et al., 2009) was used for the
232 overview maps in Fig. 2 as well as for the insert maps of the seismic imagery.

233

234 **3.2 Seismic imagery**

235 The parametric sediment sub-bottom profiler (Parasound) system (PS) can be
236 considered as a very high-resolution single channel seismic system. The Parasound
237 emits two frequencies of 18 and 22 kHz (see Hübscher et al., 2010, and references there
238 in). The parametric effect creates a narrow beam 4 kHz and 40 kHz signal within an
239 opening angle of 4.5°. The sampling frequency of the raw data is 96 kHz. In opposite to,
240 e.g., airgun seismics, the wavelet is released as "pulse trains". This means that follow-
241 up wavelets are emitted before a sea floor reflection has returned to the transducer.
242 Therefore, sea floor multiples do not necessarily correspond to twice the two-way travel
243 time (TWT) of the sea floor reflection, as known from conventional seismic.

244 The 4 kHz signal reveals a wave length of ~0.4 m penetrates the sea floor and is
245 appropriate for subbottom profiling. Depending on the acoustic impedance of the

246 sediments near the sea floor, the Parasound signal penetrates several tens of meters
247 into the sea floor and allows the resolution of layers with a thickness of very few tens of
248 centimeters. Due to the narrow beam angle diffraction hyperbola are pretty much
249 reduced if compared to classical 3.5 khz systems, which allows the data to be described
250 and interpreted in the same way as is common for migrated multi-channel seismic
251 profiles.

252 After bandpass filtering, the data is shifted in the frequency domain so that the lower cut-
253 off frequency is at the zero hertz position. Afterwards the data is transformed back into
254 the time domain with a lower sampling frequency. However, in the data available for this
255 study, the phase information was not stored, so that processing of the data is not
256 possible as it is for conventional seismic data. To compensate for the contrast between
257 the reflection amplitude from the sea floor and those from the subsurface, the amplitudes
258 are clipped during processing. An average background noise is determined from data
259 samples above the sea floor and subtracted from the data. It is in the nature of
260 Parasound data that topographic differences are usually much greater than the
261 penetration depth, so sediment structures may be difficult to discern in the images.
262 Therefore, some Parasound profiles are additionally shown as so-called “flattened
263 profiles”. In plotting these flattened profiles, the first arrival, which is the sea floor
264 reflection, runs horizontally. The variation of the water depth is therefore balanced.
265 Parasound data have been plotted with the SESuite (courtesy Hanno Keil, Univ. of
266 Bremen).

267 All Parasound profile are labeled with a water depth calculated with a rounded velocity
268 of an acoustic wave in water (1500 m/s), so the water depth is reasonably correct. It
269 seems likely, that the velocity increases slightly with depth due to compaction, so the
270 thickness of sedimentary layers is presumably underestimated and the deviation
271 increases with burial depth and compaction. The depth to reflections below sea floor are
272 calculated with a velocity of 1500 m/s to sea floor and 1500-1800 m/s below sea floor.
273 Those depth values are named “total depth”, are rounded to full 5 m and the uncertainty
274 is estimated to be $\pm 5\text{m}$, which is good enough for the discussion in this study.
275 Stratigraphic correlation between individual profiles was done with KINGDOM software
276 by IHS Markit.

277 Fig. 2b shows the M94 cruise track with the accomplished Parasound profiles, as well
278 as the core sites. The profiles stretch for ~ 150 km across the northern Campeche Bank.

279 Due to the lack in signal penetration, the profiles further south do not contribute to this
280 study.

281

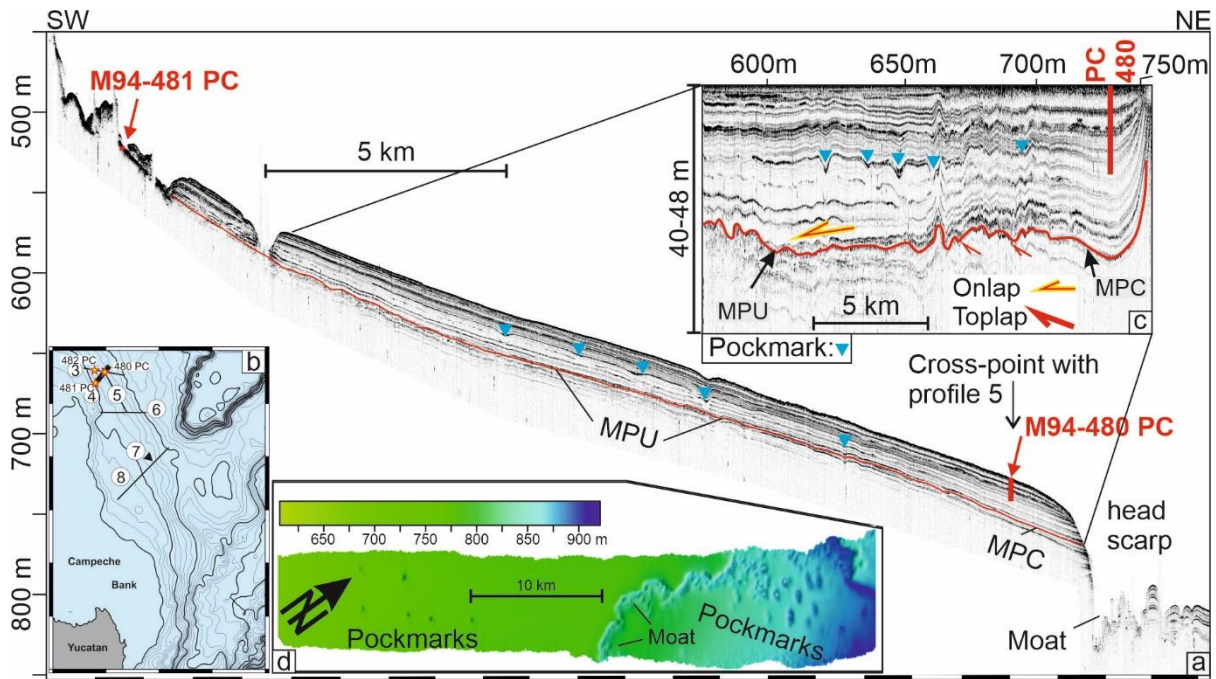
282 **3.3 Core sites**

283 During research cruise M94, piston corers (PC) with core barrel lengths between 10 and
284 20 m were run. Although sea floor sediments were extremely hard to penetrate, and ship
285 maneuvering was difficult due to up to 4 kn current speed, three deployments along the
286 profile in Fig. 2 were successful.

287 Cores M94-480 PC and M94-481 PC were taken along the SW-NE striking profile 5,
288 which well reflects the sedimentary features known from the M78/1 campaign (Hübscher
289 et al., 2010; Fig. 3). Piston core M94-480 PC (23°48.141N 87°0.868W) was recovered
290 from intermediate depths (~730 m) from the northeastern Campeche Bank penetrating
291 the layered sequence of coarse to middle foraminiferal oozes, which become finer at
292 greater depth (Fig. 4). Core recovery was ~12.2 m revealing undisturbed sediments of
293 excellent quality (Appendix 2). Core M94-480 PC ended up in a horizon that reveals
294 pockmarks (Fig. 4c).

295 The second 2.5 m long piston corer M94-481 PC (23°39.997N 87°7.284W) from the
296 northern Campeche Bank transect is from ~521 m water depth, located in the mounded
297 Campeche CWC complex (Fig. 4a). Core M94-481 PC mainly consists of an intercalated
298 sequence of light foraminiferal ooze and sand, and darker foraminifera-rich
299 shale/mudstone, reflecting glacial/interglacial-related sedimentological changes. Below
300 this sequence at ~2.3 m core depth, the lithology changes into a very coarse-grained,
301 diagenetically concreted sediment with sand-sized grains cemented into even larger
302 particles ranging from a few millimeters to several centimeter. Large brachiopods up to
303 2-3 cm in length are abundant. The contact to the upper sediment is sharp.

304



305
 306 Fig. 4: (a) Parasound profile 4 (thick black line in b) with red line marking the Mid-
 307 Pleistocene Unconformity (MPU), which transforms into the correlated conformity
 308 (MPC). Piston core locations M94-480 PC and -481 PC and penetration depth are
 309 indicated. A black arrow marks the cross-point with profile 5 at site M94-480 PC. Core
 310 length calculated with 1.8 m/ms (see chapter 5 for discussion). For location see (b). (c)
 311 Flattened Parasound profile in detail. Blue arrows mark pockmarks. Note that the up-
 312 warping of the reflections at the north-eastern end of the flattened profile results from
 313 the truncation at the head scarp only. (d) Multi-beam (SIMRAD EM122) data showing
 314 pockmarks and moat along the head scarp. VE = vertical exaggeration.

315
 316 The third piston core M94-482 PC (23°49.155N 87°7.752 W; ~7.8 m core recovery) was
 317 retrieved from ~630 m water depth, on the profile accomplished during M78 by Hübscher
 318 et al. (2010) (Fig. 3). Core M94-482 PC reveals the same sedimentary sequences as
 319 core M94-480 PC (Appendix 2), with a better preservation of the uppermost sediments.

320
 321 **3.4 Shipboard Core Logging: MINOLTA Color-Scanning**
 322 The MINOLTA CM-600d hand-held spectrophotometer was used onboard for color
 323 scanning of the freshly recovered sediment cores. The measurement of the light
 324 reflectance was done on the sediment surfaces of opened core sections. The average
 325 sample spacing is 2 cm. Before placing the Minolta device on the sediment core, the
 326 sediment surface was covered with clean and clear polyethylene foil and smoothed in
 327 order to avoid the inclusion of air bubbles at the foil-sediment interface. The

328 spectrophotometer was calibrated to avoid any variation in color measurements due to
329 the environmental (temperature, humidity, background light) and industrial variations.
330 Before the measurement of each core segment, the device was calibrated for black color
331 once using “zero-calibration” as well as for white color reflections. The spectrum of the
332 reflected light was measured by a multi-segment light sensor over a wavelength
333 spectrum from 400 to 700 nm at a 10 nm pitch. The variation in the illumination from the
334 device pulsed xenon arc lamp was automatically compensated by a double-beam
335 feedback system.

336 Routinely, the reflection data and standard color measurements were taken at 1 cm
337 steps and were automatically recorded and processed by the software MINOLTA
338 SpectraMagic v.2.3. The data are displayed in the L*, a* and b* CIELAB color
339 coordinates. The L*-value represents brightness on a non-linear scale and can be
340 directly correlated to grey value measurements. The a*-values indicate the relationship
341 between green and magenta and the b*-value reflects blue/yellow colors.

342

343 **3.5 Foraminiferal Stable Oxygen and Carbon Isotopes**

344 Stable oxygen ($\delta^{18}\text{O}$) isotope analyses were performed on a ThermoScientific MAT 253
345 mass spectrometer with an automated Kiel IV Carbonate Preparation Device at
346 GEOMAR. The isotope values are calibrated versus the NBS19 (National Bureau of
347 standards) carbonate standard and an in-house standard (“Standard Bremen”). Isotope
348 values presented in the delta-notation are reported in permil (‰) relative to the VPDB
349 (Vienna Peedee Belemnite) scale. The analytic precision is 0.06‰ for $\delta^{18}\text{O}$ and <0.03‰
350 for $\delta^{13}\text{C}$.

351 $\delta^{18}\text{O}$ measurements were made at 5 cm sample spacing for cores M84-480 and 482,
352 and 2-3 cm sample spacing for core M84-481. $\delta^{18}\text{O}$ measurements were made on 2–3
353 specimens of the endobenthic foraminiferal species *Uvigerina* spp. from the 250–500
354 μm size fraction. The size fraction was chosen to eliminate redeposited tests of smaller
355 specimens that may cause a bias of the benthic isotope signal (Lutze et al., 1979).
356 According to Shackleton and Hall (1984), *Uvigerina* $\delta^{18}\text{O}$ values appear to be in
357 equilibrium with seawater $\delta^{18}\text{O}$.

358 Additionally, $\delta^{18}\text{O}$ measurements were made on ~6 specimens of the planktonic
359 foraminiferal species *Globigerinoides ruber* (white). The specimens are taken from the
360 narrow-spaced size 355-400 μm size fraction in order to prevent bias due to ontogenetic
361 variations (Lin et al., 1997). Due to its nearly uniform annual occurrence (Tedesco and

362 Thunell, 2003), *G. ruber* shells are a standard tool for reconstructing past oceanic
363 surface hydrography conditions, especially for glacial/interglacial changes in low-
364 latitudes (Flower et al., 2004; Reissig et al., 2019; Nürnberg et al., 2021).

365

366 **3.6 ⁸⁷Sr/⁸⁶Sr Method**

367 Sr isotope ratios (⁸⁷Sr/⁸⁶Sr) of a brachiopod shell remain and enclosed residual sediment
368 were determined by thermal ionization mass spectrometry (TIMS, TRITON,
369 ThermoFisher Scientific) at GEOMAR. After segmentation of the specimen with a hand
370 hold diamond blade saw the thickest part of the well-preserved shell remain was
371 detached and rigorously purified from the matrix by diamond dental driller under
372 binocular control down to sub-mm scale pristine fragments. Additionally, on mm scale
373 two distinct spots of the consolidated, underlying and shell-attached residual sediment
374 were sub-sampled directly as powder with a diamond dental driller. All three samples
375 dissolved completely in 2.25 N HNO₃ without siliciclastic remains. Under clean lab
376 conditions they were dried down and the actual SrSpec resin (Eichrom Technologies)
377 based extraction, purification and measurement routines described in Schmidt et al.
378 (2019) were applied. The measured isotope ratios were session specific normalized to
379 the NIST SRM 987 value of 0.710248 according to Howarth and McArthur (2004) at a
380 repeatability of ± 0.000006 (2SD, n=2). Potential influences of ⁸⁷Rb interferences on
381 ⁸⁷Sr/⁸⁶Sr isotope ratios were eliminated by combining the highly selective Sr-Spec resin
382 and Rb/Sr-discriminating TIMS preheating procedures with the static mode
383 measurement of ⁸⁵Rb simultaneously with the Sr masses 84, 86, 87, and 88 for optional
384 Rb/Sr corrections. As performance monitor an aliquot of the IAPSO seawater standard
385 accompanied the whole procedure and resulted in 0.709173 ± 0.000008 (2 SEM) and
386 acceptable accordance to a reference value of 0.709175 for modern seawater (Howarth
387 and McArthur, 2004).

388

389 **4. Results**

390 **4.1 Bathymetry**

391 The Campeche Bank plateau reveals water depths of less than 100 m and a dip angle
392 of <0.2° (Fig. 2). The 100 m and 200 m depth contours along the eastern bank form a
393 nearly 200 km long arcuate terrain step with slope values up to 3°. As indicated by the
394 increasing distance between the isobaths (Fig. 2b), the slope dip is flattened in water

395 depth between 300 m and 600 m. In contrast to the 100 m and 200 m isobaths, the 600
396 m to 1000 m isobaths are convex-shaped downslope.

397

398 **4.2 Seismic imagery**

399 The Parasound profile 3 (Fig. 3) is a re-processed version of the data that were shown
400 and described by Hübscher et al. (2010; their Fig. 9). In water depth above 520 m, the
401 strong sea floor reflection allows no signal penetration. Below, the build-ups (~520-600
402 m water depth) further downslope are attributed to the CWC (*Lophelia*). As already
403 mentioned by Hübscher et al. (2010), an unconformity and correlated conformity
404 separates wavy reflections beneath from sub-parallel strata above. According to the
405 hypothesis to test, the unconformity developed in the mid Pleistocene, why the following
406 labels were chosen (Fig. 3): MPU = Mid Pleistocene Unconformity; MPC = Mid
407 Pleistocene Correlated Conformity, and MPU/C = the combined seismic interface.

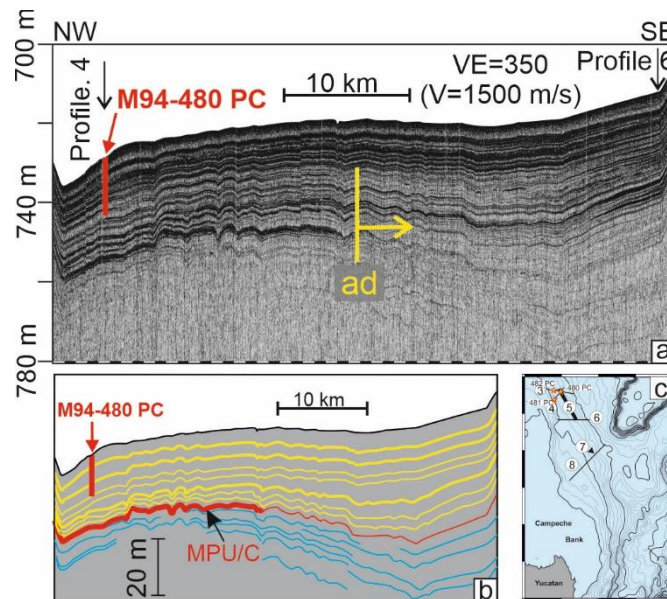
408 The most basin-ward toplap beneath the MPU/C in a present day water depth of ~660
409 m and 680 ± 5 m total depth marks the lateral transition from MPU to MPC. In a total
410 depth of ~655 m, the lowermost reflection above the MPU onlaps against it. In the
411 flattened profile (Fig. 3c), the onlap appears as a downlap.

412 In order to link the new data from the M94 campaign to observations made by Hübscher
413 et al. (2010) during the M78 expedition, the northernmost M94-profile 4 (Fig. 4) crosses
414 the M78-profile 3, striking SW-NE and perpendicular to the continental slope. Stratified
415 sediment sequences are evident below a water depth of ~520 m. Laterally traceable
416 sediments are present only below ~570 m water depth. A (head) scarp at ~750 m water
417 depth limits the occurrence of these deposits further downslope. As in profile 3, the MPU
418 changes to the MPC at ~660 m water depth and 685 ± 5 m total depth. Both, the layers
419 below the MPU/C and approximately the lower half of the sedimentary sequence above
420 reflect rather diffusely. In contrast, the reflection horizons in the upper half are sharp and
421 continuous. Also similar to the profile 3, the lowermost reflection horizon above the MPU
422 onlaps the unconformity. Lateral thickness variations become less the more upslope
423 they are.

424 Circular fluid escape structures (pockmarks) are present on the sea floor, but also buried
425 (Figs. 4c, d). Above the scarp, pockmarks at the sediment surface reveal depths of up
426 to ~40 m and diameters of ~200–260 m. Below the scarp, the pockmarks are elongated
427 (Fig. 4d). Cross-sections of the buried pockmarks can be seen best in the flattened

428 profile (Fig. 4c) and along a reflection horizon with an enhanced reflection amplitude. A
429 moat channel runs in front of the scarp.

430



431

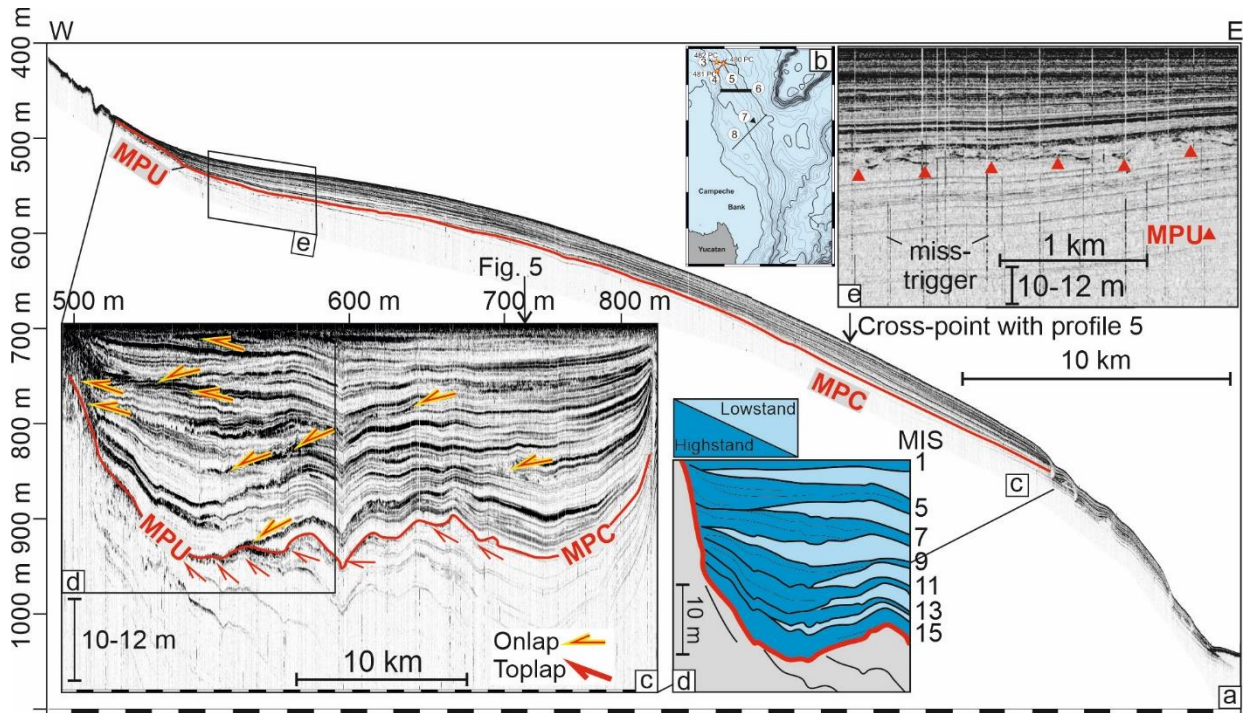
432

433 *Fig. 5: (a) Parasound profile 5 and (b) according line drawing. Red line in (b) marks Mid-*
434 *Pleistocene Unconformity and correlated conformity (MPU/C). PC480 labels piston core*
435 *M94-480 PC, which is also the cross-point (black arrow) with the Parasound profile 4.*
436 *Core length calculated with 1.8 m/ms (see chapter 5 for discussion). The cross-point*
437 *with the Parasound profile 6 (black arrow to the right) is at the southeastern end of the*
438 *profile. Note the southeastward amplitude decrease (ad) of reflections beneath ~12 m*
439 *in the middle of the profile. VE = vertical exaggeration.*

440

441 The almost 50 km long Parasound profile 5 runs in water depths of ~705-740 m almost
442 parallel to the bathymetric contour and rather perpendicular to Parasound profiles 3 and
443 4. The reflections are divergent to the southeast. Reflection terminations against MPU/C
444 are not visible. The reflection amplitudes of the MPU/C abruptly decrease towards the
445 SE, which occurs approximately, where the slope gradient flattens between 100 and 500
446 m water depth (Fig. 2b). The same applies to reflections in the lower half of the overlying
447 layers. Reflections beneath the MPU/C are wavy and diverge southwards. Reflections
448 directly above the MPU/C are also wavy. In a depth of ca. 12 m beneath the sea floor,
449 reflection coefficients and thickness undulations generally decrease towards the SE.

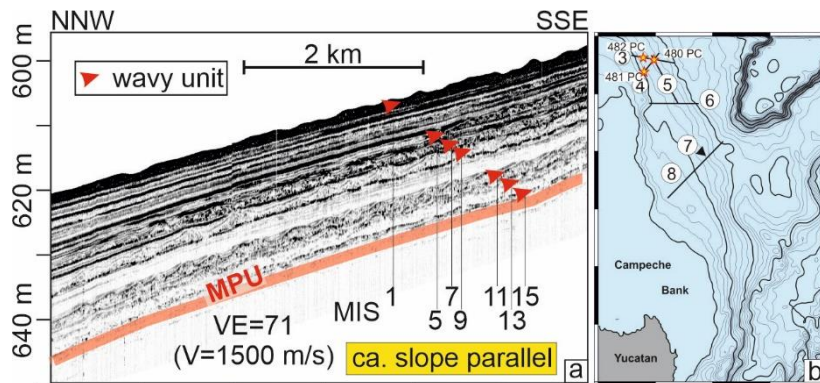
450



451
 452
 453 Fig. 6: (a) Parasound profile 6 running perpendicular to the continental slope. For
 454 location see insert map (b). Red line = Mid-Pleistocene Unconformity (MPU) and
 455 Correlated Conformity (MPC). Black arrow = cross-point with profile 5. (c) Flattened
 456 profile. Red arrows = onlaps and downlaps. (d) Line drawing with interpreted sea level
 457 highstand (dark blue), lowstand deposits (light blue) and suggested correlation with
 458 MIS. (e) Enlargement from upper slope. VE = vertical exaggeration.

459
 460 The dip profile 6 is 45 km long and reveals a reflection pattern similar to profiles 3 and
 461 4, which are 30-40 km further north. Resolvable strata start to occur below 500 m water
 462 depth. The MPC could be stratigraphically linked to profile 3 and 4 by strike profile 5. In
 463 addition, the lowermost or most basinward toplap marks the transition from the MPU to
 464 the MPC at ~680 m water depth and 710±5 m total depth. As seen best in the flattened
 465 profile (Fig. 6c), several onlap and downlap terminations are present above the MPU.
 466 The identification of reflection terminations allows recognizing 13 individual depositional
 467 units above the MPU, all marked in blue. Seven units onlap the MPU (dark blue), the
 468 other six are intercalated (light blue). In the shallower part (510-520 m water depth), the
 469 MPU separates reflections of low amplitude (below) from those with higher amplitudes.
 470 The blow-up in Fig. 6e elucidates the wavy truncation along the MPU.
 471 Seventy kilometers further to the south, a blow-up of the NNW-SSE-striking profile 7
 472 elucidates where the overburden of the MPU condenses. The sea floor and the

473 uppermost less than a meter-thick unit is wavy, and so are six further units above the
 474 MPU. Between the uppermost and the 2nd wavy unit an approximately 8 m thick unit with
 475 parallel and continuous reflections is present.
 476

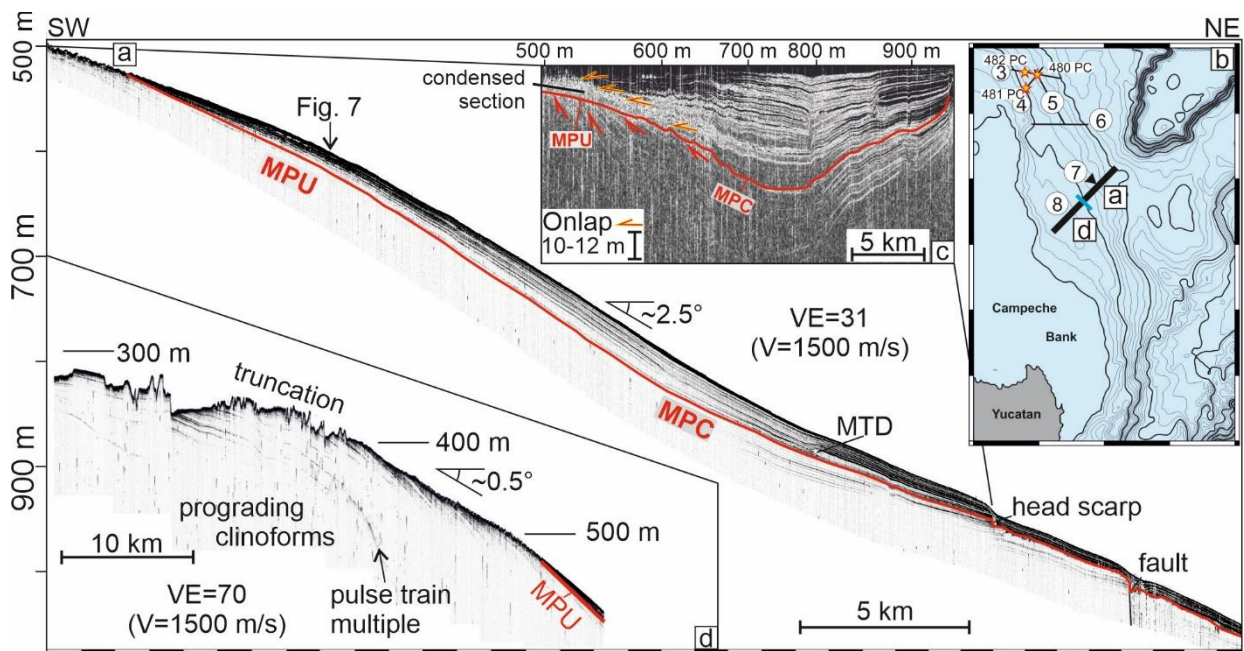


477
 478 *Fig. 7: (a) Parasound profile 7 almost parallel to the contour. (b) The profile 7 is too short*
 479 *to be resolved in the insert map. It runs almost parallel to the slope. The black triangle*
 480 *marks, where the profile stops at profile 8. Red line = Mid-Pleistocene Unconformity*
 481 *(MPU). Red arrows = wavy horizons and suggested correlation with MIS. VE = vertical*
 482 *exaggeration.*

483
 484 The southernmost dip profile 8 elucidates the slope deposits where the dip angle of the
 485 upper slope is minimal ($\sim 0.5^\circ$) (Fig. 8a, b). The transition from MTC to MTU occurs ca.
 486 at 630 m water depth and 660 ± 5 m total depth. The imaged strata below form oblique
 487 clinoforms, which are thickest at ~ 750 m water depth. The resolved strata top lap against
 488 the MPU upslope and converged further downslope. A diffusely reflecting layer a few
 489 meters thick, whose internal structure cannot be resolved, overlies the MPU upslope
 490 from about 600 m water depth. Younger units onlap against this diffusely reflecting layer
 491 but terminate upslope at ca. 520 m. Generally and along the entire profile, the strata
 492 overlying the MPU/C represent sigmoidal clinoforms. The lowermost clinoform onlaps
 493 the MPU at 600 m water depth and ca. 20 m beneath sea floor. At the upper
 494 slope, prograding sigmoidal clinoforms truncated in water depths shallower than 400 m
 495 (Fig. 8d).

496
 497 **4.3 Chronostratigraphy of sediment cores**
 498 The stratigraphic framework of cores M94-480 PC, -481 PC and -482 PC is based on a
 499 combination of stable oxygen isotope stratigraphy, orbital tuning, core correlation of
 500 sediment color data, and $^{87}\text{Sr}/^{86}\text{Sr}$ radiometric dating.

501



502

503 Fig. 8: (a) Parasound profile 8. Red line = Mid-Pleistocene Unconformity (MPU) and
504 Correlated Conformity (MPC). Black arrow = cross-point with profile 7. For location see
505 insert map (b). (c) Flattened profile with red arrows marking tolap terminations. The
506 signal to noise ratio of internal reflection amplitudes is rather small. In order to identify
507 reflection terminations and to distinguish between the MPU and the MPC, the grey scale
508 colors are inverted. (d) Upslope prolongation of (a). Note the sea floor "pulse-train"
509 multiple (see chapter 3.2 for explanation) and the different vertical exaggeration (VE)
510 compared to (a).

511

512 4.3.1 Strontium isotopes

513 The determined $^{87}\text{Sr}/^{86}\text{Sr}$ ratios of 0.709168 (± 0.000008) for the brachiopod shell
514 fragment and almost identical to each other values of 0.709157 (± 0.000009) and
515 0.709159 (± 0.000009) for the underlying residual sediment are overlapping within
516 uncertainty. Especially taking into account the extreme similarity of the two latter implies
517 a systematic difference to the shell fragment. Note, the given uncertainties include the
518 propagation of the normalization repeatability (2SD level) on the 2 SEM uncertainty of
519 the single sample measurements.

520 In order to extract potential age information from these marine carbonates the strontium
521 isotope stratigraphy (SIS) approach according to Howarth and McArthur (2004) and the
522 given data base therein is applied. Table 1 provides the transfer of $^{87}\text{Sr}/^{86}\text{Sr}$ ratios into
523 mean SIS ages and of their uncertainties into asymmetric age ranges. The latter are

524 unfortunately large for the context of this study due to the shallow slope of marine Sr
525 isotope evolution in the related time interval.

526 Nevertheless, a maximum age of 0.83 Ma is implied for a hiatus provoking current
527 regime and the related unconformity in the sediment record. The residual structure of
528 this enclosed carbonate sediment matrix is dating the shielding brachiopod to be syn- to
529 post-hiatus emplaced. Therefore, its SIS systematic indicates a maximum age of 0.57
530 Ma for the re-occurrence of a depositional regime and its sediment record investigated
531 in this study. Consequently, this age represents also the set point for estimates of the
532 minimum duration of the hiatus (0.83-0.57 Ma), which falls into the MPT.

533

534 *Table 1: Transfer of $^{87}\text{Sr}/^{86}\text{Sr}$ ratios into mean SIS ages and uncertainties. Numbers in*
535 *brackets refer to the following remarks: (1) $^{87}\text{Sr}/^{86}\text{Sr}$ normalized on NIST-SRM-987*
536 *ratio of 0.710248 according to Howarth and McArthur (2004). (2) Uncertainty applied for*
537 *SIS age range determination based on propagation of normalization 2 SD on*
538 *measurement 2 SEM. (3) 0.709175 reference values for modern seawater according*
539 *Howarth and McArthur (2004).*

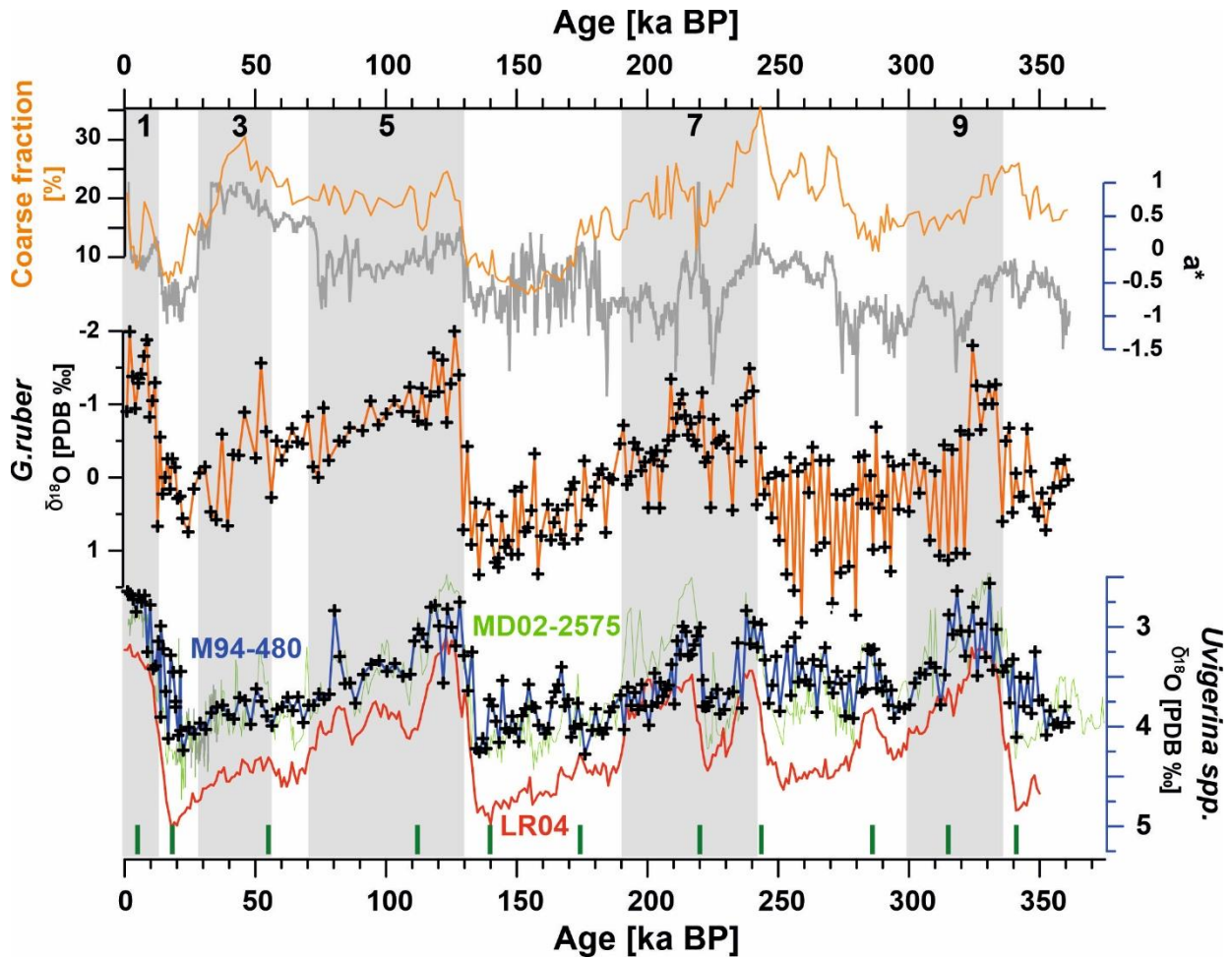
| | | | | SIS- Look-up 2004 | min age | max age |
|---|--------------|-------------------------------------|-----------|-------------------------|---------|---------|
| Sample ident | lab code | $^{87}\text{Sr}/^{86}\text{Sr}$ (1) | \pm (2) | mean age (Ma) | (Ma) | (Ma) |
| M94-481-PC-brachiopod-enclosed matrix 1 | 207-13 | 0.709157 | 0.000009 | 0.59 | 0.28 | 0.83 |
| M94-481-PC-brachiopod-enclosed matrix 2 | 208-13 | 0.709159 | 0.000009 | 0.55 | 0.23 | 0.78 |
| M94-481-PC-brachiopod-shell2 | 209-13 | 0.709168 | 0.000008 | 0.26 | recent | 0.57 |
| (3) IAPSO-modern seawater std. | session-rel. | 0.709173 | 0.000008 | | | |
| NIST SRM-987: of session / n=2 / 2 SD | session-rel. | 0.710248 | 0.000006 | | | |

540

541 **4.3.2 Oxygen isotope stratigraphy and core correlation of sediment color data**

542 The chronostratigraphy of core M94-480 PC is based on the graphic correlation of the
543 benthic $\delta^{18}\text{O}$ curve (*Uvigerina* spp.) with the stacked $\delta^{18}\text{O}$ reference record (LR04) of
544 Lisiecki and Raymo (2005) using the software AnalySeries (Fig. 9). Twelve tie lines were
545 used to tie the benthic $\delta^{18}\text{O}$ record to the reference record. The correlation between
546 LR04 and M94-480 is high ($r^2 = 0.7$) and supports the established chronology. High
547 benthic $\delta^{18}\text{O}$ values commonly refer to glacial conditions. The marine oxygen isotope
548 stages (MIS) were identified following the standard $\delta^{18}\text{O}$ nomenclature proposed by Prell
549 et al. (1986) and Tiedemann et al. (1994).

550

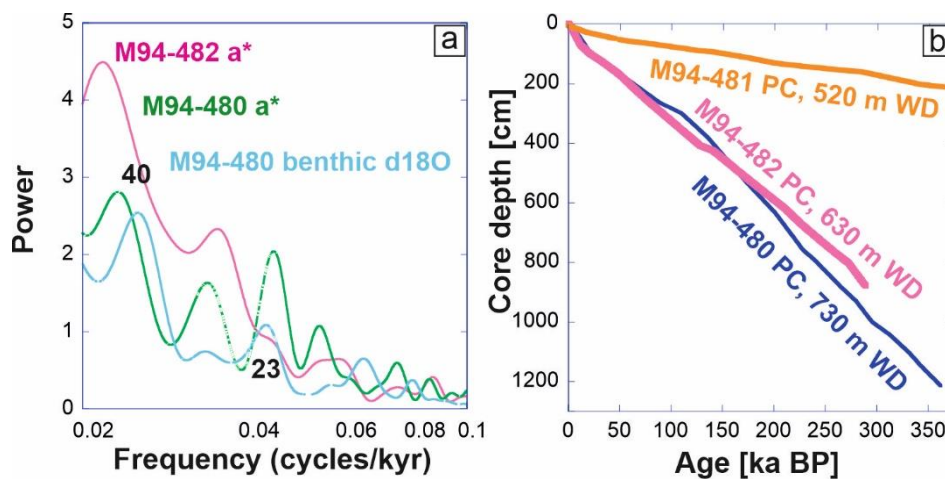


551
 552 Fig. 9. Chronostratigraphy of core M94-480 PC from Yucatan Strait, 23°48.141N
 553 87°0.868W, 730 m water depth. Bottom: Benthic stable oxygen isotope record ($\delta^{18}\text{O}$ in
 554 ‰ VPDB) over the last ~360 kyr. The stratigraphic framework is based on tuning the
 555 benthic $\delta^{18}\text{O}_{U.peregrina}$ record to the global benthic reference stack LR04 (Lisiecki and
 556 Raymo, 2005). Green vertical lines mark tie lines between both records. Further support
 557 of the age model comes from the tight match to the benthic $\delta^{18}\text{O}_{U.peregrina}$ record of core
 558 MD02-2575 from the northern Gulf of Mexico, for which a strong response to cyclic
 559 fluctuations in Earth's precession and obliquity was proven (Nürnberg et al., 2008).
 560 Middle: Planktonic $\delta^{18}\text{O}_{G.ruber}$ record (in ‰ VPDB) of core M84-480 PC. Top: Coarse
 561 grain fraction (>63 μm) and high resolution a^* -record of core M94-480 reflecting the
 562 relationship between green and magenta, which is used to establish the age model for
 563 adjacent core M94-482 PC. Interglacial periods are shaded and marine oxygen isotope
 564 stages (MIS) are indicated by black numbers.

565
 566 The stratigraphical framework of core M94-480 covers the last ~360 kyrs, showing
 567 typical glacial/interglacial $\delta^{18}\text{O}$ variability and amplitudes in both the benthic and the

568 planktonic (*G. ruber*) isotope records. The benthic $\delta^{18}\text{O}$ record is further congruent to
 569 the benthic $\delta^{18}\text{O}$ record of core MD02-2575 from the northern Gulf of Mexico (Nürnberg
 570 et al., 2008), for which a strong response to cyclic fluctuations in Earth's orbital
 571 parameters was proven (Nürnberg et al., 2008). Similarly, the B-Tukey frequency
 572 spectrum of the core M94-480 benthic $\delta^{18}\text{O}$ record reveals dominant cyclicities of 40 kyr
 573 and 23 kyr as a response to cyclic fluctuations in the Earth's orbital parameters obliquity
 574 and precession (Fig. 10).

575



576

577

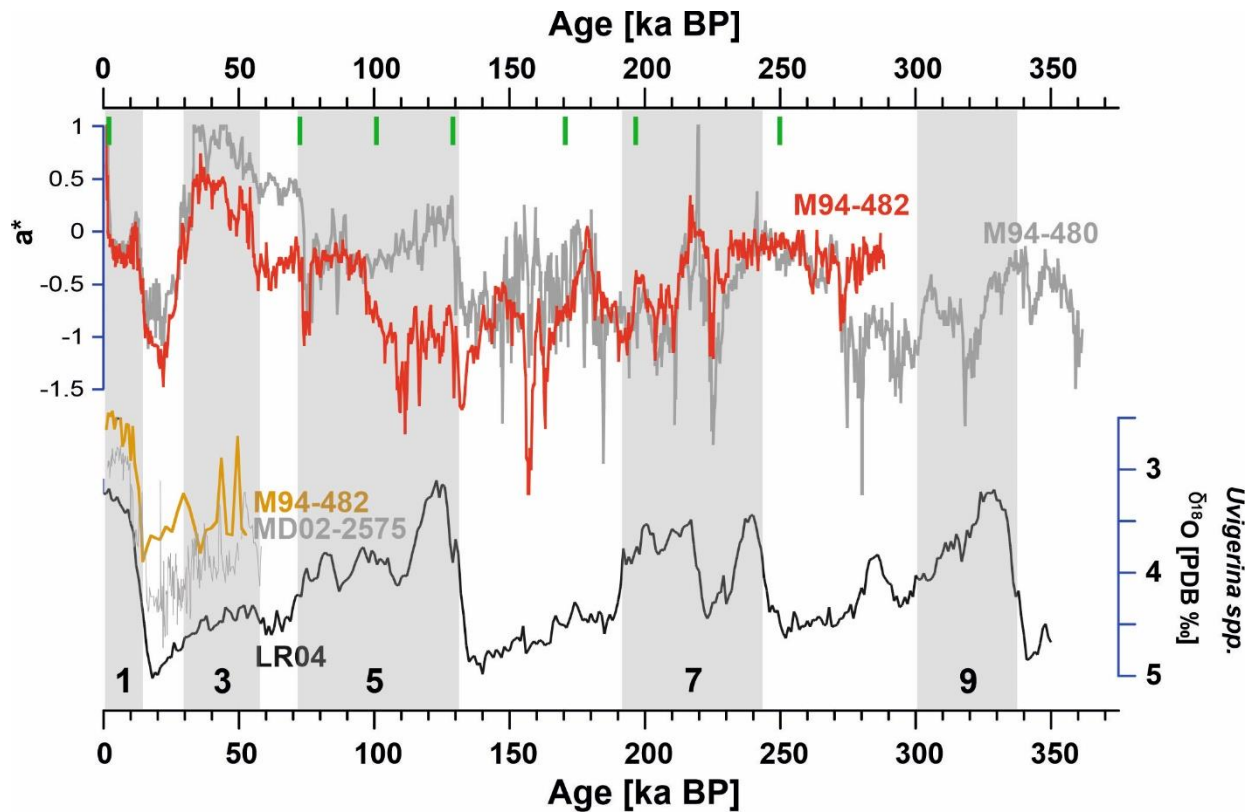
578 *Fig. 10. (a) The B-Tukey frequency spectra of the different proxy data point to orbital*
 579 *forcing. Most pronounced cyclicities of 40 kyr and 23 kyr as a response to cyclic*
 580 *fluctuations in the Earth's orbital parameters obliquity and precession occur in the*
 581 *benthic $\delta^{18}\text{O}_{U.peregrina}$ record (light blue). The frequency spectra of color a* variations in*
 582 *cores M94-480 PC (green) and M94-482 PC (orange) are less distinct due to the blurry*
 583 *character of the color records. (b) Depth/age diagrams for cores M94-480 PC (blue), -*
 584 *481 PC (orange), and -482 PC (pink) revealing decreasing sedimentation rates with*
 585 *decreasing water depths on the western slope of Yucatan Strait.*

586

587 The glacial/interglacial pattern is not such obvious in the a*-record of core M94-480 (Fig.
 588 9), and the cyclicities of 40 kyr and 23 kyr are notable but not concise (Fig. 10).
 589 Nonetheless, the a*-record of core M94-480 is useful to establish a tight correlation to
 590 core M94-482 PC.

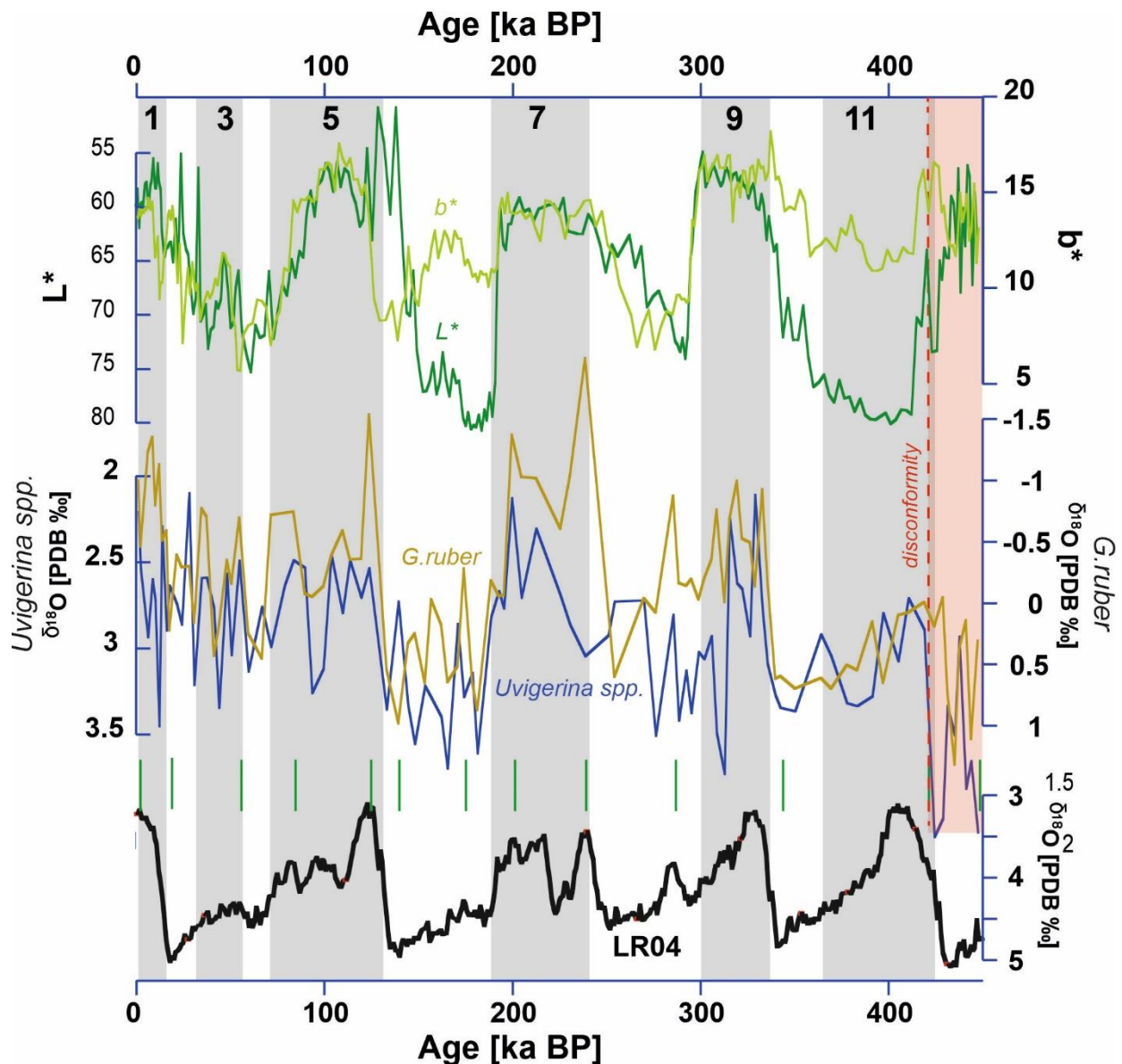
591 For core M94-482 PC, we mainly used the highly variable a*-record as age constraint,
 592 as it is rather similar to the a*-record of the stratigraphically well-classified core M94-480
 593 PC. The visual correlation of both records afforded 7 tie-lines and resulted in a

594 correlation with $r^2 = 0.5$ (Fig. 11). Low a^* -values mostly but not consistently relate to
 595 glacial time periods. Benthic $\delta^{18}\text{O}$ across the uppermost 1.8 m of core M94-482 revealing
 596 a typical glacial/interglacial $\delta^{18}\text{O}$ amplitude were visually correlated to the LR04 (Lisiecki
 597 and Raymo, 2005) and MD02-2575 (Nürnberg et al., 2008) reference records (Fig. 11),
 598 further supporting the established core chronology.
 599



600
 601 *Fig. 11. Chronostratigraphy of core M94-482 from Yucatan Strait, 23°49.155N 87°7.752*
 602 *W, 630 m water depth. Top: Visual correlation of the a^* -record (red) to the a^* -record of*
 603 *core M94-480 (gray), which serves as stratigraphically classified reference record (c.f.*
 604 *Fig. 9). Green vertical lines mark tie-lines between the records. Bottom: Further support*
 605 *of the age model in the youngest section comes from the correlation of the benthic*
 606 *$\delta^{18}\text{O}_{U.peregrina}$ record (orange) to reference sites MD02-2575 from the northern Gulf of*
 607 *Mexico (Nürnberg et al., 2008; gray) and LR04 (Lisiecki and Raymo, 2005; black).*

608
 609



610
611

612 Fig. 12. Chronostratigraphy of core M94-481 from Yucatan Strait, 23°39.997N
 613 87°7.284W, 521 m water depth. Bottom: Global benthic $\delta^{18}\text{O}$ reference stack LR04
 614 (Lisiecki and Raymo, 2005; black). Middle: The stratigraphic framework is based on
 615 tuning the planktonic $\delta^{18}\text{O}_{G.ruber}$ record (in ‰ VPDB; orange) of core M84-481 to the
 616 global benthic $\delta^{18}\text{O}$ reference stack LR04. Green vertical lines mark tie lines between
 617 the records. The correlation is largely supported by the benthic $\delta^{18}\text{O}_{U.peregrina}$ record of
 618 core M84-481 (blue). Top: L^* and b^* -records of core M84-481 reflecting
 619 glacial/interglacial changes from MIS1 to MIS11. A prominent disconformity is dated to
 620 ~425ka BP (red dashed line). Below, the strongly lithified coarse-grained sediment
 621 contains large brachiopod shells dated with $^{87}\text{Sr}/^{86}\text{Sr}$.

622 The stratigraphical range of core M94-482 covers the last ~288 kyrs, showing
623 glacial/interglacial variability in the sedimentary pattern. Due to the blurry character of
624 the core M94-482 a^* -record, the B-Tukey spectrum is not clear, although spectral
625 maxima are close to 40 kyr and 23 kyr cyclicities (Fig. 10).

626 For core M94-481 PC, the stratigraphic interpretation of the foraminiferal $\delta^{18}\text{O}$ signal is
627 challenging, because foraminifers are generally rare and partly absent in some core
628 intervals. Also, the $\delta^{18}\text{O}$ signals and amplitudes in planktonic and benthic foraminifers
629 do not vary consistently. Biostratigraphical information implies that the base of core M94-
630 481 is younger than 890 ka BP (see above) suggesting that the prominent variations in
631 sediment color L^* and b^* (Fig. 12) may be related to glacial/interglacial variability. We
632 therefore visually tuned the $\delta^{18}\text{O}_{G.ruber}$ record of core M94-481 to the LR04 $\delta^{18}\text{O}$
633 reference stack of Lisiecki and Raymo (2005), thereby applying 13 tie-lines and receiving
634 a correlation of $r^2 = 0.6$. Light foraminiferal $\delta^{18}\text{O}$ values are consistently related to
635 interglacial time periods. According to the resulting age model, the M94-481 core covers
636 glacial/interglacial changes from MIS1 to 11, with the prominent disconformity at 2.3 m
637 core depth achieving an age of ~425 ka BP. This is consistent to the $^{87}\text{Sr}/^{86}\text{Sr}$ age
638 estimate of maximum 570 ka BP for a brachiopod shell from right below the
639 disconformity.

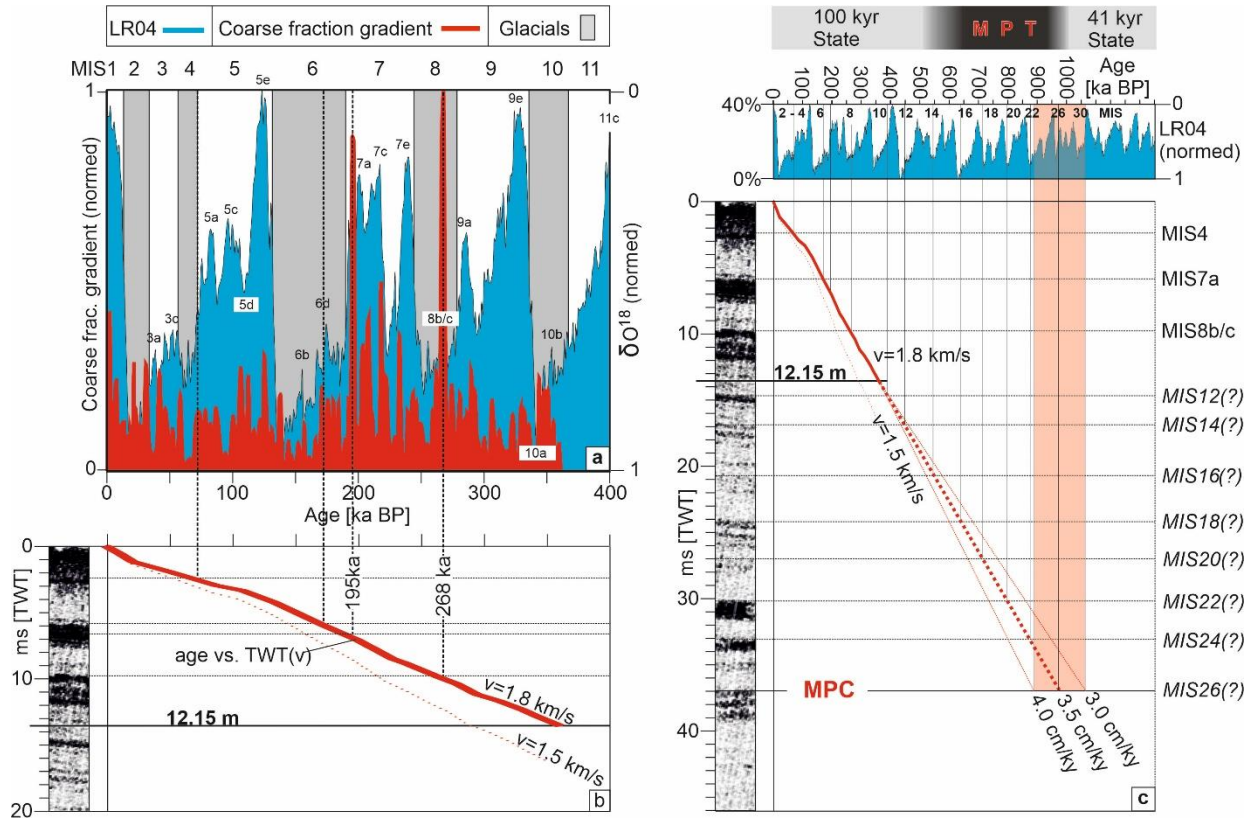
640 The age-depth relationships for cores M94-480 PC and -482 PC appear continuous and
641 without significant disturbances. The average sedimentation rate is $\sim 3 \pm 1$ cm/kyr, being
642 slightly higher in the deeper core M94-480 PC. Considerably lower sedimentation rates
643 of 0.6 ± 0.3 cm/kyr are reconstructed for core M94-481 PC. This is the shallowest and
644 shortest core, but reaches farthest back in time.

645

646 **4.3.3 Core-seismic integration**

647 The age of the MPU/C can in principle be estimated by extrapolation of the previously
648 determined sedimentation rates, provided that the age-depth function can be applied to
649 the Parasound data. However, the rounded sound velocity of water (1500 m/s) usually
650 used in all profile figures cannot simply be transferred to the sediment cores for accurate
651 extrapolation. For the integration of stratigraphical core and Parasound information, we
652 assume that the relative changes in the coarse (grain) fraction in sediment core M94-
653 480 PC cause the acoustic impedance contrasts. The coarse fraction $>63 \mu\text{m}$ from core
654 M94-480 PC was determined approximately every 5 centimeters (top Fig. 9). Each value
655 was then assigned an age, based on the chronostratigraphy established in Fig. 9 (c.f.

656 Fig. 10b). In order to constrain the correlation between relative seismic reflection
 657 amplitudes with assumed acoustic impedance changes, the vertical gradient of the
 658 coarse fraction was further determined by calculating the difference between adjacent
 659 samples.



660
 661
 662 *Fig. 13: (a) In the upper figure, the normalized gradient of the coarse fraction of sediment*
 663 *core M94-480 PC (Fig. 9) and the normalized LR04 $\delta^{18}O$ reference record (Lisiecki and*
 664 *Raymo, 2005) are plotted vs. time and MIS. Odd MIS are indicated by grey background*
 665 *color. MIS substages after Railsback et al. (2015). In the lower figure, reflection*
 666 *amplitudes are correlated with these data. The conversion from age-to-depth (Fig. 10b)*
 667 *to age-to-TWT was performed with a constant sound of 1800 m/s. (b) Extrapolation of*
 668 *age-TWT function yields an age of the MPC between ~900 and 1050 ka BP. See text*
 669 *for discussion.*

670
 671 In Fig. 13a, the coarse fraction gradient is plotted against time and the LR04 $\delta^{18}O$
 672 reference record. For further consideration, it is unimportant whether the gradient is
 673 positive or negative, since the phase information of the Parasound data was not
 674 recorded. Because absolute values are not required for neither the coarse fraction
 675 gradient nor for $\delta^{18}O$ values both sets of numbers were normalized.

676

677

678

679 The further procedure assumes that the coarse fraction represents a proxy for the
680 sediment density. In this case, the gradient of the coarse fraction is a proxy for the
681 reflection coefficient. The higher the gradient, the higher the reflection coefficient.
682 Consequently, the coarse fraction gradient should correlate with the reflection
683 amplitudes in the Parasound data. Next, the age-depth function was converted into an
684 age-twt function with various sound velocities. Since no further constrains were
685 available, the simple assumption of a constant velocity seemed to be the most
686 reasonable approach. When choosing a sound velocity of 1800 m/s, the top of the high
687 amplitude reflection at 6 ms and that at 10 ms TWT correlate quite well with the coarse
688 fraction gradient at MIS 4-5a, 6d, 7a and 8b/c (Fig. 13 a). Depth-conversion with 1800
689 m/s yields a maximum age of ca. 360 kyrs for the base of the core, which is congruent
690 to the age that was estimated from the stratigraphic analysis.

691 For the extrapolation of the core data down to the MPU/C we used sedimentation rates
692 between 3 and 4 cm/kyr, because the sedimentation rate for the last 50,000 years in the
693 lower core range (361-314 kyr) varied between these rates (Fig. 13b). As can be seen
694 in Fig. 9, the coarse grain fraction is larger during the sea level highstands (interglacials)
695 than during the lows (glacials). The number of changes between weakly and more
696 reflective time intervals in the Parasound data roughly corresponds to the number of
697 glacial/interglacial changes.

698

699 **5. Interpretation and Discussion**

700 **5.1 Overall setting**

701 Generally, seaward concave, arcuate isobaths in the upslope domain in conjunction with
702 convex isobaths further downslope are typical of headwalls or head scarps of mass
703 transport complexes (MTC; e.g., Bull et al., 2009, and references there in). As there is
704 much evidence that the Chicxulub impact on the northwestern Campeche Bank, western
705 Florida shelf, and Texas coast resulted in large-scale mass remobilization (Paull et al.
706 2014; Sanford et al., 2016, Pag 2017; 2022; Guzmán-Hidalgo et al., 2021), we suggest
707 that the eastward concave, arcuate 100 m – 300 m isobaths represent the headwall
708 domain of an about 150 km broad MTC (Fig. 1b). Consequently, the lobe shaped 600 m
709 – 1000 m characterizes the top surface of the toe domain. Without any further seismic

710 reflection data we unfortunately cannot rule out that the 100–300 m isobath represents
711 the edge of, e.g., a back-stepping carbonate platform or rim reef.

712 The convex shaped deposits downslope of the headwall and on top of the MTC can be
713 considered as an infilling or plastered drift (Faugères and Stow, 2008; Rebesco et al.,
714 2014), which Hübscher et al. (2010) already postulated for the western Florida Shelf. In
715 addition, there is some local evidence for gas escape structures (surface and buried
716 pockmarks; Fig. 4). Pockmarks in shallow deposits of carbonate platforms are generally
717 rare, because the organic carbon content is always very low (Betzler et al., 2011, and
718 references there in). Land et al. (1995) described circular structures with a hybrid
719 genesis controlled by submarine fresh water discharge and carbonate solution along the
720 Florida margin. If the pockmark result from expelling fluids, the source should be below
721 the carbonate platform, because any organic carbon content of the Campeche
722 carbonate banks is not reported.

723

724 **5.2 Geological age constrains**

725 The M94-480 PC core-seismic integration implied that at the core site the MPC is about
726 28 m (calculated from 37 ms TWT and $v=1.8$ m/s) and consequently
727 730 m + 28 m = 758 m beneath present day seafloor. Hence, deposition on the MPC
728 started in that depth right before or during the early MPT (900-1050 Ma; MIS 23-24).

729 The correlation between Parasound data, core derived age models and coarse fraction
730 is built on simplified assumptions. E.g., reflection amplitudes may be well related to
731 carbonate lithification or cementation, compaction etc.. Those factors would also
732 influence the sound velocity in the sediments. Therefore, the following discussion builds
733 on the age estimation that the MPC coincides with the early MPT.

734 The age constraints for M94-481 PC are less consistent. Sr-isotope analysis of M94-481
735 PC samples (521 m water depth plus max. 2.3 m sediments) implies a maximum age of
736 0.83 Ma for the top of the condensed section and onset of non-deposition (hiatus). When
737 the deep base level was above this core site since MIS15, sedimentation commenced.
738 However, because of the insufficient vertical mapping of the MPC in the Parasound data,
739 the exact assignment of the condensed layer to the MPC is unclear at this position and
740 water depth.

741

742 **5.3 Geophysical age constrains (upper slope)**

743 A seismo-stratigraphic interpretation of Parasound profiles 6 and 7 further constrains the
744 age of upper slope deposits. In profile 6 (Fig. 6), deposits above the MPU and in water
745 depths of 500-600 m can be divided into 15 alternating sequences, one of which
746 alternately terminates against the MPU, and the one above it onlaps against the lower
747 unit. Since the uppermost or youngest unit terminates against the MPU, this can be
748 considered characteristic of highstand deposition. This interpretation would be
749 consistent with the highstand shedding model (Schlager et al., 1994) and a relatively
750 shallower base-level as a result of relative sea level. If the base-level drops during glacial
751 and relative sea level lows, the depositional space shifts downslope. If this assignment
752 of sedimentary units to glacial/interglacial cycles is correct, seven highstand units and
753 six lowstand units can be identified (Fig. 6c, d). Consistently, the unit directly overlying
754 the MPU would be assigned to MIS 15 and the MPU would be assigned to MIS 16. This
755 corresponds to the Sr analysis.

756 As the uppermost unit of slope-parallel profile 7 (Fig. 7) is characterized by sediment
757 waves, we conclude that these sediment waves are typical of sea level highstand
758 conditions, similar as during the Holocene. Up to seven wavy units, presumably dune
759 fields, can be identified above the MPU. When these highstand deposits are assigned
760 to interglacial MIS, it follows that the MPU formed during glacial MIS 16 and is overlain
761 by interglacial MIS15 deposits. A consequence of this model would be that a thicker than
762 average (ca. 6-7 m) deposit would have been deposited here during MIS2-4. Betzler et
763 al. (2014) observed similar dune fields or sediment waves at the western Great Bahamas
764 Bank, the crests of which strike along the contours. In our study, the sediment waves
765 are only observed locally in strike profile 7, which is why an interpretation as cyclic steps
766 seems not appropriate.

767

768 **5.4 Deep base level control on MPU/C**

769 We need to address the issue how the transition from unconformity (MPU) to conformity
770 (MPC) took place. Hübscher et al. (2010) explained the MPU in profile 3 (Fig. 3) by an
771 abruptly strengthened bottom flow that eroded concordantly overlying layers. As
772 Hübscher et al. (2010) already noted, a short-lived paleoceanographic event during the
773 MPT is not yet documented. There is also no evidence for mass wasting, which could
774 explain the MPU as a basal shear-surface (decollement) of a slump or slide. We hence
775 argue that the onset of sedimentation further downslope is a function of both increasing
776 current velocities and deep base level. As summarized e.g. by Chen et al. (2019), strong

777 deep-water bottom currents are often related to result from THC- or wind-driven currents
778 (e.g., Rebesco, 2005), benthic storms (e.g., Gardner et al., 2017), intermittent
779 mesoscale eddies (e.g., Liang and Thurnherr, 2011; Serra et al., 2010; Rubino et al.,
780 2012; Thran et al., 2018; Chen et al., 2019), and internal waves (Reiche et al., 2016;
781 Quayyum et al., 2017; Miramontes et al., 2020).

782 In the Yucatan Channel, the highest current velocities are in the central part of the
783 Yucatan Current and decrease towards the slopes of the Yucatan peninsula and Cuba
784 (Sheinbaum et al., 2002). Hübscher et al. (2010) previously showed that in the Yucatan
785 Strait, hydroacoustically detectable sediments do not occur until below 550-600 m. Since
786 the LC continues northwards, it is likely that the LC and episodically separating warm-
787 core rings (eddies) generally control deposition and non-deposition along the eastern
788 Campeche Bank. The internal waves at the TACW/AAIW-boundary and in water depth
789 of ~520-540 m as postulated by Hebbeln et al. (2014) control the deep base level itself,
790 as significant sedimentation currently only occurs below this depth. According to this
791 rather conceptual explanation, the presence of internal waves is not crucial, since the
792 deep base level can simply be explained by a decrease of the flow velocity of the LC.
793 Eddies and benthic storms tend to be episodic events, however, on geologic time scales
794 they can be considered quasi-continuous processes. In this regard, deep eddies
795 generally act in water depths >1000 m (Oey, 2008) and can thus be ruled out as
796 causative for deep base level. The same applies to mesoscale eddies as described, e.g.,
797 by Chen et al. (2019), which also affect continental slopes in water depth of >1000 m.

798

799 **5.5 Deep base level fluctuations**

800 The duration of the deep base level fall that caused the forced regression systems tract-
801 like offlapping clinoforms beneath the MPU is unconstrained. Since the supra-MPU/C
802 strata comprise several glacial/interglacial cycles, a single eustatic sea level fall cannot
803 be accounted for the deep base level fall by more than 100 m, since the offlapping strata
804 were deposited during the deep base level fall. Further, this offlapping sediment package
805 of the toplapping clinoforms beneath the MPU is much thicker than the several 100 kyrs
806 old overburden of the MPU/C. Hence, the offlapping sediment package comprises at
807 least several 100 kyrs as well (Figs. 6c, 8c). In contrast to hydrodynamic explanations,
808 a deep base level fall or rise can theoretically also be explained by subsidence or
809 tectonically controlled uplift. However, as no such studies exist, a tectonic control of the
810 here described processes can be ruled out.

811 It is reasonable to assume that the deep base level fall resulted from the LC
812 intensification during the narrowing and closure of the Panama Isthmus in the middle or
813 late Pliocene. For a detailed discussion of different time constraints for the closure see
814 O’Dea et al. (2016) and references therein. The truncation of prograding clinoforms
815 above 400 m water depth and the lack of sedimentation since then (Fig. 8) can also be
816 interpreted by the onset of the LC or its amplification.

817 The overlapping supra MPU-strata at the upper slope (Figs. 6a, 8a) imply a deep base
818 level rise. This is consistent with the age models discussed previously, which dated the
819 MPC to the beginning of the MPT, and the sediments above the MPU on the upper slope
820 to the outgoing MPT or to the time after. Similar to the Levant margin (eastern
821 Mediterranean), the deep base level rise created a sigmoidal sediment body that reveals
822 characteristics comparable to Transgressive Systems Tracts (Hübscher et al., 2016).
823 That the sedimentary package above the MPU/C generally terminates as onlap against
824 the MPU, but was deposited during several glacial cycles, provides evidence of an
825 overall weakening of the flow regime along the upper slope of the eastern Campeche
826 Bank since the MPT. The uniformity of supra-MPU/C deposition suggests that the cause
827 is not a gradual decline in the shedding of more local and episodic eddies, but a
828 weakening of the contour-parallel LC. This attenuation holds on average for all other
829 fluctuations, e.g., pycnocline disappearance during glacials (Matos et al. 2017),
830 shedding of anticyclonic eddies (e.g., Oey, 2008; Nürnberg et al., 2008; Nürnberg et al.,
831 2015), but also seasonal variations (Wiseman and Dinnel, 1988; Sheinbaum et al.,
832 2002).

833

834 **5.6 Paleooceanography and Paleoclimate implications**

835 **5.6.1 MPT**

836 According to the core-seismic integration, the maximum depth of the deep base level
837 was reached at ca. 950-1100 kyr BP, i.e., at the onset of the MPT. If the deep base level
838 correlates with the water transport and associated heat transfer from the western Atlantic
839 warm water pool towards the North Atlantic via the AMOC, the mid-Pleistocene heat
840 transport was maximum ~~back~~ (?) then. Subsequently, the deep base level shifted
841 upward, implying a reduced current-related heat transfer. A close link between LC
842 strength and ocean THC is likely, as ~~the~~ for the onset of the deep base level (~950 ka
843 BP) is consistent with a major disruption of the THC system during the MPT between
844 MIS 25 and 21 at ~950 to 860 ka BP (Pena and Goldstein, 2014; Kim et al., 2021).

845 The uplift of the deep base level documents the overall weakening of the LC and thus a
846 reduction in heat transport from the Caribbean to the North Atlantic via Florida Straits,
847 which is consistent with these notions. As summarized by Pena and Goldstein (2014),
848 several authors explained the MPT by cooling of sea-surface temperatures and
849 increased high-latitude sea-ice expansion (Gildor and Tziperman, 2010; Martinez-
850 Garzia et al., 2010; McClymont et al., 2013) and/or changes in THC vigor (Raymo et al.,
851 1990).

852

853 **5.6.2 The post-MPT 100.000 yr world**

854 The seismic imagery of our study further shows that the reflection pattern above the
855 MPU/C and in water depths above ~660-680 m changes from slightly wavy to sub-
856 parallel to parallel, i.e., becoming more and more straight in the upmost layers (Figs. 3-
857 5). Averaged over astronomical cycles, this argues for a steady decrease in LC vigor.
858 The dependency of LC vigor and the net through flow via the Yucatan and Florida straits
859 on glacial/interglacial periods, however, remains a matter of debate.

860 As the highstand dune fields (Fig. 7) indicate a higher-energy depositional environment
861 than the parallel layers between them, the proposed age model in Fig. 7 implies weaker
862 bottom currents during glacials (sea level low-stands) than during the interglacials (high-
863 stands). Stieglitz et al. (2009; 2011) argued for a reduced Florida Straits transport during
864 the LGM and Younger Dryas. Based on the Nd-proxy analysis, Pena and Goldstein
865 (2014) and Kim et al. (2021) also concluded on the reduction of AMOC vigor during the
866 glacials. However, the latter observation can also be explained by the fact that a large
867 part of the northward AMOC transport during the lows does not pass through the
868 Yucatan Strait, but takes place east of the Caribbean Islands (Antilles, etc.). Brunner
869 (1984) explained higher sand contents (preferentially foraminiferal tests) in warm climate
870 sediments from the Yucatan Channel by lowered sedimentation rates due to stronger
871 winnowing of the fine grain fraction. The positive correlation between the coarse grain
872 fraction of M94-480 PC and sea level (cf. Fig. 13) can be interpreted in the same way.
873 However, this interpretation is not unambiguous, because the increased relative
874 proportion of the coarse grain fraction consisting mainly of foraminifera-during sea level
875 highstands can ~~therefore~~ also be explained by increased marine productivity.

876 In contrast, the eddy-permitting model simulations of Nürnberg et al. (2015) imply that
877 the southward shift of the Intertropical Convergence Zone and the strengthened
878 atmospheric circulation during glacial periods intensified the (wind-driven) Sverdrup

879 transport within the Subtropical Gyre (Slowey and Curry, 1995). At the same time, the
880 lowered sea level and the related smaller Yucatan Strait cross section rather caused the
881 strengthening of the Yucatan and Florida straits throughflow. In response to the stronger
882 throughflow, the LC eddy shedding in the Gulf of Mexico vanished, which would explain
883 the extreme sea surface cooling in the northern Gulf (Nürnberg et al., 2008; 2015).
884 The different notions on either glacially reduced or intensified LC flow cannot be
885 conclusively answered yet. Under the following assumptions, the flow velocity of the LC
886 must have been lower during the glacial than during the interglacial periods: If the
887 reflection patterns in Fig. 7 are interpreted correctly in terms of inferred flow velocity,
888 sealevel and climate change, if this local observation is representative of the entire
889 eastern Campeche Bank, and if the coarse grain fraction in sediment cores is a result of
890 winnowing,

891

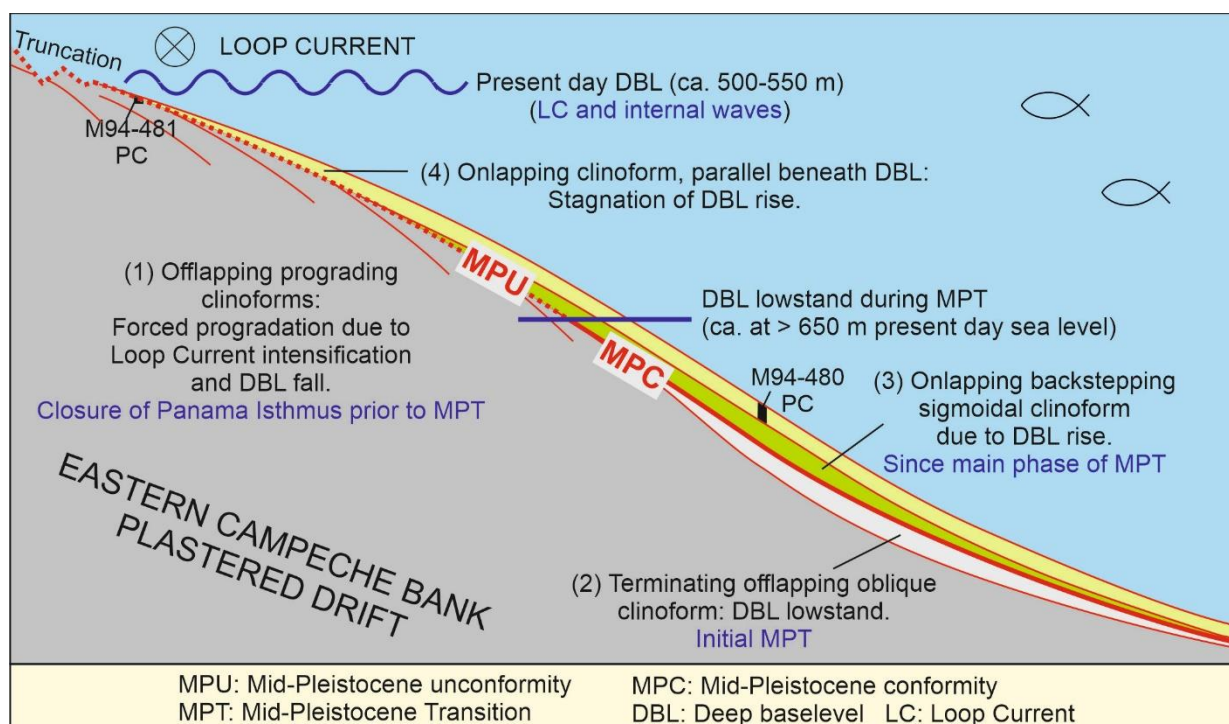
892 **6. Conclusions**

893 Similar to the northern margin of Campeche Bank, the bathymetry (Fig. 2) of the eastern
894 Campeche Bank between 22° and 23.5° north and in water depths between 100 m and
895 1000 m indicates that over a distance of about 150 km the upper slope was remobilized.
896 Since the Chicxulub impact could be shown to be the cause for similar mass failures at
897 the northern margin of Campeche Bank, it can be speculated that the impact was also
898 the cause here.

899 Approximately between 500 and 650 m present day water depth, the Parasound data
900 depict prograding and offlapping clinoforms about 20-30 m below the seafloor that are
901 similar to a forced regression systems tract well known from continental shelves (Fig.
902 14). The downslope bounding clinoform is oblique. While on continental shelves the
903 relative sea level under additional influence from the storm wave base or tides control
904 the base level, the deep base level fall here can be interpreted by LC amplifying until the
905 initial MPT. The deep base level fall led to erosion and truncation of prograding deposits
906 above 500 m. No sedimentation during MPT until MIS15 created a hiatus and condensed
907 section at the upper slope.

908 The offlaps form an unconformity (MPU) that is concordantly overlain. This sigmoidal
909 sediment sequence above resembles a transgressive systems tract. The overlying
910 sedimentary sequence retrogrades and onlaps the MPU. Below 650 m, the MPU
911 becomes its correlated conformity (MPC). In each case, the youngest seismically

912 resolved onlap is at about 500-550 m. This 20-30 m thick sigmoidal sedimentary
 913 sequence above the MPU/C represents a plastered drift.
 914 The transition from deep base level fall prior to the MPT to deep base level rise
 915 documents a weakening of the LC initially during the MPT. After the MPT, the LC
 916 continues to weaken, most prominent during glacials. Since this implies a reduction of
 917 the heat transport from the western Atlantic warm water pool into the North Atlantic and
 918 consequently up to NW Europe, the general weakening of the LC may explain the further
 919 cooling of the Northern hemisphere after the MPT.
 920



921
 922 *Fig. 14: Summary sketch, manly based on profile 8 across the central drift (Fig. 8).*
 923

924 **Declaration of competing interests**

925 The authors declare that they have no known competing financial interests or personal
 926 relationships that could have appeared to influence the work reported in this paper.

927
 928 **Data statement**

929 All data are already uploaded to PANGAEA data base and will be made public directly
 930 after publication in peer reviewed journal.

932 **Acknowledgements**

933 We thank Volker Liebtreu for the strontium dating. Volker unfortunately passed away
934 before the publication of this study. Furthermore, we thank Maria Álvarez García for the
935 bio-stratigraphic information. We like to thank captain Michael Schneider, his officers
936 and crew of RV METEOR for their support of our measurement programme. We further
937 like to thank Wolfgang Mahrle (German Federal Foreign Office) and Hubertus von
938 Römer (German Embassy Mexico City) for their great support during the diplomatic
939 clearance.

940

941 **Funding**

942 RV METEOR expedition M94 was funded by the German Research Foundation (DFG)
943 and the Federal Ministry of Education and Research (BMBF).

944

945 **References**

946 Antoine, J.W., Ewing, J.I., 1963. Seismic refraction measurements on the margins of
947 the Gulf of Mexico. J Geophys Res 68, 1975-1996

948 Amante, C. and B. W. Eakins, ETOPO1 1 Arc-Minute Global Relief Model: Procedures,
949 Data Sources and Analysis. NOAA Technical Memorandum NESDIS NGDC-24, 19 pp,
950 March 2009. Go to this web site: <http://www.ngdc.noaa.gov/mgg/global/global.html>.

951 Balsam W.L., Beeson J.P., 2003. Sea floor sediment distribution in the Gulf of Mexico.
952 Deep-Sea Research I 50, 1421-1444

953 Betzler, C., Lindhorst, S., Hübscher, C., Lüdmann, T., Fürstenau, J., 2011. Giant
954 pockmarks in a carbonate platform (Maldives, Indian Ocean). Marine Geology, 289, 1-
955 16.

956 Betzler, C., Lindhorst, S., Eberli, G., Lüdmann, T., Möbius, J., Ludwig, J., Schutter, I.,
957 Wunsch, M., Reijmer, J.J.G., Hübscher, C., 2014. Periplatform drift: The combined
958 result of contour current and off-bank transport along carbonate platforms. Geology
959 42(10), 871-874.

960 Brunner, C.A. 1984. Evidence for increased volume transport of the Florida Current in
961 the Pliocene and Pleistocene. *Marine Geology* 54, 223-235

962 Bull, S., Cartwright, J., & Huuse, M. (2009). A review of kinematic indicators from
963 mass-transport complexes using 3D seismic data. *Marine and Petroleum Geology*,
964 26(7), 1132-1151.

965 Catuneanu, O., Abreu, V., Bhattacharya, J.P., Blum, M.D., Dalrymple, R.W., Eriksson,
966 P.G., Fielding, C.R., Fisher, W.L., Galloway, W.E., Gibling, M.R., Giles, K.A., Holbrook,
967 J.M., Jordan, R., Kendall, C. G. St. C., Macurda, B., Martinsen, O.J., Miall, A.D., Neal,
968 J.E., Nummedal, D., Pomar, L., Posamentier, H.W., Pratt, B.R., Sarg, J.F., Shanley,
969 K.W., Steel, R.J., Strasser, A., Tucker, M.E., Winker, C., 2009. Towards the
970 standardization of sequence stratigraphy. *Earth-Science Rev.* 92, 1-33.

971 Emiliani, C., 1975. Paleoclimatological analysis of Late Quaternary cores from the
972 northeastern Gulf of Mexico. *Science* 189, 1083-1089

973 Ezer, T., Oey, L.-Y., Lee H.-C., Sturges, W. 2003. The variability of currents in the
974 Yucatan Channel: analysis of results from a numerical ocean model. *Journal of*
975 *Geophysical Research*, 108(C1), 3012

976 Faugères J-C, Stow DAV. 2008. Contourite drifts: nature, evolution and controls. In
977 *Contourites*, Rebesco M, Camerlenghi A (eds), *Developments in Sedimentology* 60.
978 Elsevier: Amsterdam; 257–288.

979 Flower, B.P., Hastings, D.W., Hill, H.W., Quinn, T.M., 2004. Phasing of deglacial
980 warming and Laurentide ice sheet melt water in the Gulf of Mexico. *Geology* 32(7),
981 597–600

982 Gardner, W.D., Tucholke, B.E., Richardson, M.J., Biscaye, P.E., 2017. Benthic storms,
983 nepheloid layers, and linkage with upper ocean dynamics in the western North Atlantic.
984 *Mar. Geol.* 385, 304–327.

985 Gardulski, A.F., Mullins, H.T., Weiterman, S. 1990. Carbonate mineral cycles
986 generated by foraminiferal and pteropod response to Pleistocene climate: West Florida
987 ramp slope. *Sedimentology* 37, 727-743.

988 Gardulski, A.F., Marguerite, H.G., Milsark, A., Weiterman, S.D., Sherwood, W.W. Jr.,
989 Mullins, H.T., 1991. Evolution of a deep-water carbonate platform: Upper Cretaceous

990 to Pleistocene sedimentary environments on the west Florida margin. *Marine Geology*,
991 101, 163-179

992 Gildor, H., Tziperman, E., 2010. Sea ice as the glacial cycles' climate switch: role of
993 seasonal and orbital forcing. *Paleoceanography* 15, 605–615

994 Guzmán-Hidalgo, E., Grajales-Nishimura, J.M., Eberli, G.P., Aguayo-Camargo, J.E.,
995 Urrutia-Fucugauchi, J., Pérez-Cruz, L., 2021.

996 Hebbeln, D., Wienberg, C., Wintersteller, P., Freiwald, A., Becker, M., Beuck, L., Dullo,
997 C., Eberli, G.P., Glogowski, S., Matos, L., Forster, N., Reyes-Bonilla, H., Taviani, M.,
998 2014. Environmental forcing of the Campeche cold-water coral province, southern Gulf
999 of Mexico. *Biogeosciences*, 11, 1799-1815

1000 Hönisch, B., Hemming, N. G., Archer, D., Siddall, M., McManus, J. F., 2009.
1001 Atmospheric carbon dioxide concentration across the mid-Pleistocene transition.
1002 *Science* 324, 1551–1554.

1003 Howarth, R. J. and McArthur, J. M.: Strontium isotope stratigraphy, in *A Geological*
1004 *Time Scale, with Look-up Table Version 4*, edited by: Gradstein, F. M. and Ogg, J. G.,
1005 Cambridge University Press, Cambridge, U.K., 96–105, 2004.

1006 Hübscher, C., Pulm, P., 2009. Parasound. In: J. Schönfeld, A. Bahr, B. Bannert, A.-S.
1007 Bayer, M. Bayer, C. Beer, T. Blanz, W.-C. Dullo, S. Flögel, T. Garlichs, B. Haley, C.
1008 Hübscher, N. Joseph, M. Kucera, J. Langenbacher, D. Nürnberg W.-T. Ochsenhirt, A.
1009 Petersen, P. Pulm, J. Titschack, L. Troccoli (2011) Surface and Intermediate Water
1010 hydrography, planktonic and benthic biota in the Caribbean Sea – Climate, Bio and
1011 Geosphere linkages (OPOKA) - Cruise No. M78/1 - February 22 - March 28, 2009 -
1012 Colón (Panama) - Port of Spain (Trinidad and Tobago). *METEOR-Berichte*, M78/1, 40
1013 pp., DFG-Senatskommission für Ozeanographie, DOI:10.2312/cr_m78_1

1014

1015 Hübscher, C., Dullo, C., Flögel, S., Titschack, J., Schönfeld, J. 2010. Contourite drift
1016 evolution and related coral growth in the eastern Gulf of Mexico and its gateways.
1017 *International Journal of Earth Science*, 99(1) 191-206

1018 Hübscher, C., D. Nürnberg, M. Al Hseinat, M. Alvarez García, Z. Erdem, N. Gehre, A.
1019 Jentzen, C. Kalvelage, C. Karas, B. Kimmel, T. Mildner, A. O. Ortiz, A. O. Parker, A.
1020 Petersen, A. Raeke, S. Reiche, M. Schmidt, B. Weiß, D. Wolf (2014) Yucatan

1021 Throughflow - Cruise No. M94 – March 12 – March 26, 2013 – Balboa (Panama) –
1022 Kingston (Jamaica). METEOR Berichte, M94, 32 pp., DFG-Senatskommission für
1023 Ozeanographie, DOI:10.2312/cr_m94

1024 Hübscher, C., Betzler, C., Reiche, S., 2016. Seismo-stratigraphic evidences for deep
1025 base level control on middle to late Pleistocene drift evolution and mass wasting along
1026 southern Levant continental slope (Eastern Mediterranean). *Journal of Marine and*
1027 *Petroleum Geology* 77, 526-534.

1028 Imbrie, J., Berger, A., Boyle, E.A., Clemens, S.C., Duffy, A., Howard, W.R., Kukla, G.,
1029 Kutzbach, J., Martinson, D.G., McIntyre, A., Mix, A.C., Molino, B., Morley, J.J.,
1030 Peterson, L.C., Pisias, N.G., Prell, W.L., Raymo, M.E., Shackleton, N.J., Toggweiler,
1031 J.R., , 1993. On the structure and origin of major glaciation cycles. Part 2: the 100,000-
1032 year cycle. *Paleoceanography*, 8 699-735

1033 Johns, W.E., Townsend, T.L., Fratantoni, D.M., Wilson, W.D., 2002. On the Atlantic
1034 inflow to the Caribbean Sea. *Deep Sea Research Part 1: Oceanographic Research*
1035 *Papers*.

1036 Kaiser, E. A., Caldwell, A., & Billups, K. (2019). North Atlantic upper-ocean
1037 hydrography during the mid-Pleistocene transition evidenced by *Globorotalia*
1038 *truncatulinoides* coiling ratios. *Paleoceanography and Paleoclimatology*, 34, 658–671.
1039 <https://doi.org/10.1029/2018PA003502>

1040 Kim, J., Goldstein, S.L., Pena, L.D., Jaume-Seguí, M., Knudson, K.P., Yehudai, M.,
1041 Bolge, L., 2021. North Atlantic Deep Water during Pleistocene interglacials and
1042 glacials. *Quaternary Science Reviews* 269, 107146,
1043 <https://doi.org/10.1016/j.quascirev.2021.107146>

1044 Land, L.A., Paull, C.K., Hobson, B., 1995. Genesis of a submarine sinkhole without
1045 subaerial exposure: Straits of Florida. *Geology* 23(10), 949-951

1046 Liang, X., Thurnherr, A.M., 2011. Subinertial variability in the deep ocean near the East
1047 Pacific rise between 9° and 10°N. *Geophys. Res. Lett.* 38.

1048 Lin, H.L., Peterson, L.C., Overpeck, J.T., Trumbore, S.E., Murray, D.W., 1997. Late
1049 Quaternary climate change from $\delta^{18}\text{O}$ records of multiple species of planktonic
1050 foraminifera: high resolution records from the anoxic Cariaco Basin, Venezuela.
1051 *Paleoceanography* 12, 415–427.

1052 Lutze, G. F., Sarnthein, M., Koopmann, B., Pflaumann, U., Erlenkeuser, H. and
1053 Thiede, J., 1979. "Meteor" Core 12309: Late Pleistocene reference section for
1054 interpretation of the Neogene of Site 397. In: U. von Rad, W. B. F. Ryan, et al., Init.
1055 Rep. Deep Sea Drill. Proj., 47A: 727--739.

1056 Lisiecki, L.E., Raymo, M.E., 2005. A Pliocene–Pleistocene stack of 57 globally
1057 distributed benthic $\delta^{18}\text{O}$ records. *Paleoceanography* 20, PA1003.
1058 doi:10.1029/2004PA001071

1059 Lynch-Stieglitz, J., Curry, W.B., Lund, D.C., 2009. Florida straits density structure and
1060 transport over the last 8,000 years. *Paleoceanography and Paleoclimatology* 24(3).
1061 doi.org/10.1029/2008PA001717

1062 Lynch-Stieglitz, J., Schmidt, M.W., Curry, W.B., 2011. Evidence from the Florida Straits
1063 for Younger Dryas ocean circulation changes. *Paleoceanography and*
1064 *Paleoclimatology* 26(1). <https://doi.org/10.1029/2010PA002032>

1065 Martínez-García, A. Rosell-Melé, A., McClymont, E.L., Gersonde, R., Haug, G.H.,
1066 2010. Subpolar Link to the Emergence of the Modern Equatorial Pacific Cold Tongue.
1067 *Science* 328, 1550–1553

1068 Martini, E., 1971. Standard Tertiary and Quaternary calcareous nannoplankton
1069 zonation. *Proc. Planktonic Conf.*, 2nd, Roma, 1970, 2: 739--785.

1070 Matos, L., Wienberg, C., Titschack, J., Schmiedl, G., Frank, N., Abrantes, F., Cunha,
1071 M.R., Hebbeln, D., 2017- Coral mound development at the Campeche cold-water coral
1072 province, southern Gulf of Mexico: Implications of Antarctic Intermediate Water
1073 increased influence during interglacials. *Marine Geology* 392, 53-65.

1074 McClymont, E.L., Sosdian, S.M., Rosell-Melé, A., Rosenthal, Y., 2013. Pleistocene
1075 sea-surface temperature evolution: Early cooling, delayed glacial intensification, and
1076 implications for the mid-Pleistocene climate transition. *Earth Sci. Rev.* 123, 173–193.

1077 Merino, M., 1997. Upwelling on the Yucatan Shelf: hydrographic evidence. *J. Mar.*
1078 *Syst.* 13, 101–121. [http://dx.doi.org/10.1016/S0924-7963\(96\)00123-6](http://dx.doi.org/10.1016/S0924-7963(96)00123-6).

1079 Miramontes, E., Jouet, G., Thereau, E., Bruno, M., Penven, P., Guerin, C., Le Roy, P.,
1080 Droz, 1286 L., Jorry, S.J., Hernández-Molina, F.J., Thiéblemont, A., Silva Jacinto, R.,
1081 Cattaneo, A. 2020. The impact of internal waves on upper continental slopes: insights

1082 from the Mozambican margin (southwest Indian Ocean). *Earth Surf. Process.*
1083 *Landforms*, 45, 1469–1482.

1084 Molinari, R.L., Johns, E., Festa, J.F., 1990. The annual cycle of meridional heat-flux in
1085 the Atlantic Ocean at 26.5-degrees-N. *Journal of Physical Oceanography* 20, 476–482

1086 Mudelsee, M., Schulz, M., 1997. The mid-Pleistocene climate transition: onset of 100
1087 ka cycle lags ice volume buildup by 280 ka, *Earth Planet. Sci. Lett.* 151 117-123.

1088 Nürnberg, D., Ziegler, M., Karas, C., Tiedemann, R., Schmidt, M., 2008. Interacting
1089 Loop Current variability and Mississippi River discharge over the past 400 kyr. *Earth*
1090 *and Planetary Science Letters* 272, 278-289

1091 Nürnberg, D., Bahr, A., Mildner, T., Eden, C., 2008. Loop Current Variability—Its
1092 Relation to Meridional Overturning Circulation and the Impact of Mississippi Discharge.
1093 In: Schulz, M., Paul, A., (eds.). *Integrated Analysis of Interglacial Climate Dynamics*
1094 (INTERDYNAMIC), Springer Briefs in Earth System Sciences, 55-62. DOI
1095 10.1007/978-3-319-00693-2_10

1096 Nürnberg, D., Bahr, A., Mildner, T. C. and Eden, C., 2015. Loop Current variability - its
1097 relation to meridional overturning circulation and the impact of Mississippi discharge.
1098 In: *Integrated Analysis of Interglacial Climate Dynamics (INTERDYNAMIC)*, ed. by
1099 Schulz, M. and Paul, A.. Springer Briefs in Earth System Sciences . Springer, Cham,
1100 pp. 55-62. ISBN 978-3-319-00692-5 DOI 10.1007/978-3-319-00693-2_10.

1101 Nürnberg, D., Riff, T., Bahr, A., Karas, C., Meier, K., Lippold, J., 2021. Western
1102 Boundary Current in relation to Atlantic Subtropical Gyre dynamics during abrupt
1103 glacial climate fluctuations. *Global Planetary*
1104 *Change*. <https://doi.org/10.1016/j.gloplacha.2021.103497>.

1105 Nürnberg, Dirk (2022): Benthic and planktonic stable isotopes of sediment core M94-
1106 481 PC. PANGAEA, <https://doi.org/10.1594/PANGAEA.947792>

1107 Nürnberg, Dirk (2022): Sedimentation rate and color data of sediment core M94-481
1108 PC. PANGAEA, <https://doi.org/10.1594/PANGAEA.947793>

1109 Nürnberg, Dirk (2022): Benthic and planktonic stable isotopes and coarse fraction of
1110 sediment core M94-480 PC. PANGAEA, <https://doi.org/10.1594/PANGAEA.947790>

1111 Nürnberg, Dirk (2022): Sedimentation rate and color data of sediment core M94-480
1112 PC. PANGAEA, <https://doi.org/10.1594/PANGAEA.947791>

1113 Nürnberg, Dirk (2022): Benthic stable isotopes of sediment core M94-482 PC.
1114 PANGAEA, <https://doi.org/10.1594/PANGAEA.947795>

1115 Nürnberg, Dirk (2022): Sedimentation rate and color data of sediment core M94-482
1116 PC. PANGAEA, <https://doi.org/10.1594/PANGAEA.947797>

1117 O'Dea, A., Lessios, H. A. , Coates, A. G. , Eytan, R. I., Restrepo-Moreno, S. A. , Cione,
1118 A. L., Collins, L. S., de Queiroz, A., Farris, D. W. , Norris, R. D., Stallard, R. F.,
1119 Woodburne, M. O., Aguilera, O., Aubry, M.-P., Berggren, W. A., Budd, A. F., Cozzuol,
1120 M. A., Coppard, S. E., Duque-Caro, H., Finnegan, S., Gasparini, G. M., Grossman, E.
1121 L., Johnson, K. G., Keigwin, L. D., Knowlton, N., Leigh, E. G., Leonard-Pingel, J. S.,
1122 Marko, P. B., Pyenson, N. D., Rachello-Dolmen, P. G., Soibelzon, E., Soibelzon, L.,
1123 Todd, J. A., Vermeij, G. J., Jackson, J. B. C., 2016. Formation of the Isthmus of
1124 Panama. *Sci. Adv.* 2, e1600883

1125 Oey, L.-Y., Lee, H.C., Schmitz, W.J., 2003. Effects of wind and Caribbean eddies on
1126 the frequency of Loop Current eddy shedding: a numerical model study. *J Geophys*
1127 *Res* 108(C10), 3324

1128 Oey, L.-Y., 2004. Vorticity flux through the Yucatan Channel and Loop Current
1129 variability in the Gulf of Mexico. *J. Geophys. Res.* 109, C10004

1130 Oey, L., Y., 2008. Loop Current and Deep Eddies. *Journal of Physical Oceanography*,
1131 38, 1426-1447

1132 Paull, C.K., Caress, D.W., Gwiazda, R., Urrutia-Fucugauchi, J., Rebolledo-Vieyra, M.,
1133 Lundsten, E., Anderson, K., Sumner, E.J., 2014a. Cretaceous–Paleogene boundary
1134 exposed: Campeche Escarpment, Gulf of Mexico. *Marine Geology*, 357, 392–400.
1135 doi.org/10.1016/j.margeo.2014.10.002.

1136 Pena, L.D., Goldstein, S.L., 2014. Thermohaline circulation crisis and impacts during
1137 the mid-Pleistocene transition *Science* 345 (6194), 318-322. DOI:
1138 [10.1126/science.1249770](https://doi.org/10.1126/science.1249770)

1139 Piasias, N.G., Moore, T.C., 1981. The evolution of Pleistocene climate: a time series
1140 approach, *Earth Planet. Sci. Lett.* 52 450-458.

1141 Poag, C.W., 2017. Shaken and stirred: Seismic evidence of Chicxulub impact effects
1142 on the West Florida carbonate platform, Gulf of Mexico. *Geology* 45 V.11; 1011–1014
1143 doi:10.1130/G39438.1

1144 Poag, C.W., 2022, Bolide impact effects on the West Florida Platform, Gulf of Mexico:
1145 End Cretaceous and late Eocene: *Geosphere*, v. 18, no. X, 1– 27,
1146 <https://doi.org/10.1130/GES02472.1>.

1147 Prell, W.L., 1982. Oxygen and carbon isotope stratigraphy for the Quaternary of hole
1148 502B: evidence for two modes of isotopic variability, *Init. Rep. DSDP 68 (1982)* 455-
1149 464

1150 Prell, W.L., Imbrie, J., Martinson, D.G., Morley, J.J., Pisias, N.G., Shackleton, N.J.,
1151 Streeter, H.F., 1986. Graphic correlation of oxygen isotope stratigraphy application to
1152 the Late Quaternary. *Paleoceanography and Paleoclimatology*, 1(2), 137-162.

1153 Quayyum, F., Betzler, C., Cataneanu, O., 2017. The Wheeler diagram, flattening
1154 theory, and time. *Marine and Petroleum Geology* 86, 1417-1430.

1155 QGIS Development Team (2009). QGIS Geographic Information System. Open
1156 Source Geospatial Foundation Project. <http://qgis.osgeo.org>.

1157 Railsback, L.B., Gibbard, P.L., Head, M.J., Voarintsoa, N.R.G., Toucanne, S., 2015.
1158 An optimized scheme of lettered marine isotope substages for the last 1.0 million
1159 years, and the climatostratigraphic nature of isotope stages and substages.
1160 *Quaternary Science Reviews* 111, 94-106.

1161 Raymo, M.E., Ruddiman, W.F., Shackleton, N.J., Oppo, D.W., 1990. Evolution of
1162 Atlantic pacific delta-C-13 gradients over the last 2.5 my. *Earth Planet Sci. Lett.* 97,
1163 353-368. [https://doi.org/10.1016/0012-821X\(90\)90051-X](https://doi.org/10.1016/0012-821X(90)90051-X).

1164 Raymo, M.E. Oppo, D.W., Curry, W., 1997. The mid-Pleistocene climate transition: a
1165 deep sea carbon isotopic perspective, *Paleoceanography* 12, 546-559.

1166 Rebesco, M., 2005. Contourites. In: Selley, R.C., Cocks, L.R.M., Plimer, I.R. (Eds.),
1167 *Encyclopedia of Geology*. Elsevier, Oxford, pp. 513–527.

1168 Rebesco, M., Hernandez-Molina, F.J., van Rooij, D., Wählin, 2014. Contourites and
1169 associated sediments controlled by deep-water circulation processes: state-of the-art
1170 and future considerations. *Mar. Geol.* 352, 111-154.

1171 Reißig, S., Nürnberg, D., Bahr, A., Poggemann, D.-W., Hoffmann, J., 2019. Southward
1172 displacement of the North Atlantic subtropical gyre circulation system during North
1173 Atlantic cold spells. *Paleoceanogr. Paleoclimatol.* 34 [https://doi.org/10.1029/](https://doi.org/10.1029/2018PA003376)
1174 2018PA003376.

1175 Rivas, D., Badan, A., Ochoa, J., 2005. The ventilation of the deep Gulf of Mexico.
1176 *Journal of Physical Oceanography* 35, 1763-1781

1177 Rubino, A., Falcini, F., Zanchettin, D., Bouche, V., Salusti, E., Bensi, M., Riccobene,
1178 G., De Bonis, G., Masullo, R., Simeone, F., Piattelli, P., Sapienza, P., Russo, S.,
1179 Platania, G., Sedita, M., Reina, P., Avolio, R., Randazzo, N., Hainbucher, D., Capone,
1180 A., 2012. Abyssal undular vortices in the Eastern Mediterranean basin. *Nat. Commun.*
1181 3, 834.

1182 Ruddiman, W.F., Raymo, M.E., Martinson, D.G., Clement, B.M., Backman, J., 1989.
1183 Pleistocene evolution: northern hemisphere ice sheets and North Atlantic Ocean,
1184 *Paleoceanography*, 4 353-412.

1185 Sanford, J.C., Snedden, J.W., Gulick, S.P.S., 2016. The Cretaceous-Paleogene
1186 boundary deposit in the Gulf of Mexico: large-scale oceanic basin response to the
1187 Chicxulub impact. *J. Geophys. Res. Solid Earth* 121 (3), 1240–1261.
1188 <https://doi.org/10.1002/2015JB012615>.

1189 Schlager, W., Reijmer, J.J.G., Droxler, A., 1994. Highstand shedding of carbonate
1190 platforms. *Journal of Sedimentary Research* 64 (3b), 270–281.

1191 Schmidt, C., Hensen, C., Wallmann, K., Liebetrau, V., Tatzel, M., Schurr, S. L.,
1192 Kutterolf, S., Haffert, L., Geilert, S., Hübscher, C., Lebas, E., Heuser, A., Schmidt,
1193 M., Strauss, H., Vogl, J. and Hansteen, T. (2019) Origin of high Mg and SO₄ fluids in
1194 sediments of the Terceira Rift, Azores – indications for caminite dissolution in a waning
1195 hydrothermal system. *Open Access Geochemistry, Geophysics, Geosystems*, 20. DOI
1196 10.1029/2019GC008525.

1197 Schmieder, F., v. Dobeneck, T., Bleil, U. 2000. The Mid-Pleistocene climate transition
1198 as documented in the deep South Atlantic Ocean: initiation, interim state and terminal
1199 event. *Earth and Planetary Science Letters*, 179 (3-4), 539-549. doi:10.1016/S0012-
1200 821X(00)00143-6

1201 Schmitz, W.J., Richardson, P.L. (1991) On the Sources of the Florida Current. Deep-
1202 Sea Research 38,379-409

1203 Schott, F.A., Lee, T.N., Zantopp, R.. 1988. Variability of Structure and Transport of the
1204 Florida Current in the Period Range of Days to Seasonal. Journal of Physical
1205 Oceanography 18(9), 1209-1230

1206 Serra, N., Ambar, I., Boutov, D., 2010. Surface expression of Mediterranean Water
1207 dipoles and their contribution to the shelf/slope-open ocean exchange. Ocean Sci.
1208 Discuss. 6, 191–209.

1209 Shackleton, N.J. and Hall, M.A., 1984. Oxygen and carbon isotope stratigraphy of
1210 Deep Sea Drilling Project Hole 552A: Plio-Pleistocene glacial history. D-G. Roberts. D.
1211 Schnitker et al. Initial Reports of the Deep Sea Drilling Project, 81,599-609. U.S. Govt.
1212 Printing Office, Washington.

1213 Sheinbaum, J., Candela, J., Badan, A., Ochoa, J., 2002. Flow structure and transport
1214 in the Yucatan Channel. Geophysical Research Letters, 29, NO. 3, 1040,
1215 10.1029/2001GL013990

1216 Slowey, N.C., Curry, W.B., 1995. Glacial/interglacial differences in circulation and
1217 carbon cycling within the upper western North Atlantic. Paleoceanography and
1218 Paleoclimatology 10(4). doi:10.1029/95PA01166

1219 Sturges, W., Evans, J.C., 1983. On the variability of the Loop Current in the Gulf of
1220 Mexico. Journal of Marine Research 41, 639-653

1221 Tachikawa, K., Rapuc, W., Dubois-Dauphin, Q., Guihou, A., Skonieczny, C., 2020.
1222 Reconstruction of ocean circulation based on neodymium isotopic composition:
1223 potential limitations and application to the Mid-Pleistocene transition. Oceanography.
1224 <https://doi.org/10.5670/oceanog.2020.205>.

1225 Tedesco, K.A. and Thunell, R.C., 2003. Seasonal and interannual variations in
1226 planktonic foraminiferal flux and assemblage composition in the Cariaco Basin,
1227 Venezuela. J. Foraminiferal Res. 33 (3), 192–210.

1228 Thran, A.C., Dutkiewicz, A., Spence, P., Müller, R.D., 2018. Controls on the global
1229 distribution of contourite drifts: Insights from an eddy-resolving ocean model. Earth
1230 Planet. Sci. Lett. 489, 228–240.

- 1231 Tiedemann, R., Sarnthein, M., Shackleton, N.J., 1994. Astronomic timescale for the
1232 Pliocene Atlantic $\delta^{18}\text{O}$ and dust flux records of Ocean Drilling Program Site 659.
1233 *Paleoceanography and Paleoclimatology*, 9(4), 619-638.
- 1234 Uchupi, E., Emery, K.O., 1968. Structure of continental margin off Gulf Coast of United
1235 States. *Am Assoc Petroleum Geologists Bull* 52, 1162-1193
- 1236 Wiseman, Jr., W.J., Dinnel, S.P., 1988. Shelf Current Near the Mouth of the
1237 Mississippi River. *Journal of Physical Oceanography* 18(9), 1287-1291
- 1238 Zavala-Hidalgo, J., Morey, S.L., O'Brian, J.J., Zamudio, L. (2006) On the Loop Current
1239 eddy shedding variability. *Atmósfera* 19, 41-48
- 1240 Ziegler, M., Nürnberg, D., Karas, C., Tiedemann, R., Lourens, L.J., 2008. Persistent
1241 summer expansion of the Atlantic Warm Pool during glacial abrupt cold events. *Nature*
1242 *Geoscience* 1, 681-685